Structure of Hydrated Gibbsite and Brucite Edge Surfaces: DFT Results and Further Development of the ClayFF Classical Force Field with Metal−O−H Angle Bending Terms

Maxime Pouvreau,[†] Jeffery A. Greathouse,[‡] Randall T. Cygan,[‡] and Andrey G. Kalinichev*,[†]

[†]Laboratoire SUBATECH (UMR 6457), Institut Mines-Télécom Atlantique, 44307 Nantes, France
[‡]Geochemistry Department, Sandia National Laboratories, P.O Box 5800, MS 0754, Albuquerque, New Mexico 87185-0754, United States

S *Supporting Information*

ABSTRACT: Molecular scale understanding of the structure and properties of aqueous interfaces with clays, metal (oxy-) hydroxides, layered double hydroxides, and other inorganic phases is strongly affected by significant degrees of structural and compositional disorder of the interfaces. ClayFF was originally developed as a robust and flexible force field for classical molecular simulations of such systems (Cygan, R. T.; Liang, J.-J.; Kalinichev, A. G. *J. Phys. Chem. B* **2004**, 108, 1255−1266). However, despite its success, multiple limitations have also become evident with its use. One of the most important limitations is the difficulty to accurately model the edges of finite size nanoparticles or pores rather than infinitely layered periodic structures. Here we propose a systematic approach to solve this problem by developing specific metal−O−H (M−O−H) bending terms for ClayFF, $E_{bend} = k (\theta - \theta_0)^2$ to better describe the structure and dynamics of singly protonated hydroxyl groups at mineral surfaces, particularly edge surfaces. On the basis of a series of DFT calculations, the optimal values of the Al−O−H and Mg−O−H parameters for Al and Mg in octahedral coordination are determined to be $\theta_{0,AlOH} = \theta_{0,MgOH} = 110°$, $k_{AlOH} = 15$ kcal mol^{-1} rad^{-2} and $k_{MgOH} = 6$ kcal mol^{-1} rad^{-2}. Molecular dynamics simulations were performed for fully hydrated models of the basal and edge surfaces of gibbsite, $Al(OH)_3$, and brucite, $Mg(OH)_2$, at the DFT level of theory and at the classical level, using ClayFF with and without the M−O−H term. The addition of the new bending term leads to a much more accurate representation of the orientation of O−H groups at the basal and edge surfaces. The previously observed unrealistic desorption of OH_2 groups from the particle edges within the original ClayFF model is also strongly constrained by the new modification.

Gibbsite edge surface OH in *xz* plane
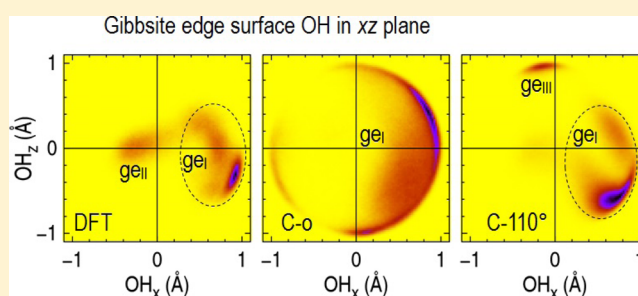
INTRODUCTION

Fundamental molecular-scale understanding of the processes occurring at mineral−water interfaces is of great importance for solving many geochemical, environmental, and technological problems.[1,2] Clay minerals attract special attention in this context.[3] They are hydrous layered aluminum silicates usually in the form of ultrafine-grained (micro to nanoscale) crystallites. Their crystal structure consists of tetrahedral (T) silicate sheets and octahedral (O) oxyhydroxide sheets, either in a 1:1 (T−O) or 2:1 (T−O−T) ratio. Isomorphic substitutions in tetrahedral and octahedral sheets (typically, Al for Si and Mg for Al, respectively) produce a wide diversity of clay mineral structures and compositions. The amount of isomorphic substitutions determines the total negative layer charge of the clay structures that is compensated by the presence of cations in the interlayer space and controls the ability of clay interlayers to hydrate and swell at specific relative humidity levels. The octahedral sheets of clays are traditionally considered to be their structural backbone, with their compositional and structural features serving as the major criteria for their

identification.[3] The capacity of clays to adsorb and immobilize extraneous species as well as their chemical stability explain wide industrial use of clays and makes them ideal candidates for a number of important applications (e.g., deep geological waste disposal, decontamination, and heterogeneous catalysis).[4]

Many of the most widely used experimental techniques to characterize clay minerals (vibrational spectroscopy, NMR, neutron scattering/diffraction, X-ray absorption/diffraction spectroscopies, and atomic force microscopy)[4] can provide significant insight regarding the structure and dynamical behavior of these materials, but it is often difficult to interpret these experimental data without having a detailed molecular-scale picture of these systems in mind. At the same time, computational molecular modeling methods, such as Monte Carlo or molecular dynamics (MD) simulations, are capable of providing direct quantitative information on a fundamental molecular scale about numerous interfacial and bulk properties

of such materials.[5] In classical simulations, interatomic forces are derived from a set of interaction energy terms often called force fields (FFs). Contrary to methods based on quantum mechanics, FFs do not treat the electronic effects explicitly, enabling the simulation of very large systems ($\sim 10^6$ atoms) and long simulation time ($\sim 10^{-6}$ s). However, the successful application of such classical simulation methods depends heavily on the quality of the FFs, whose parametrization is usually based on an empirical fit of various properties of materials (e.g., thermodynamic, structural, and spectroscopic) to available experimental data and/or to results of quantum chemical calculations.

The development of FF parameters always involves a compromise between accuracy and transferability. Several implementations of fully flexible FF models specifically designed for clays and related materials have been developed in the last two decades.[6−13] Most of these models incorporate explicit valence (bonded) parameters, and their number and complexity often restricts their applicability to a relatively limited range of well-defined crystal structures. ClayFF[1] was initially constructed to overcome this impediment by principally relying on electrostatic terms and a relatively small number of simple nonbonded Lennard-Jones parameters (to describe van der Waals interactions). Partial charges were derived from a Mulliken population analysis and an electrostatic potential fitting method from DFT (GGA) single-point calculations. Lennard-Jones parameters were assigned to metal (M) atoms by fitting the calculated crystallographic parameters to experimentally derived ones. The parametrization was based on a number of simple oxides, hydroxides, and oxyhydroxides with experimentally well-defined structures[1] and has since proven to be transferable to a wide range of inorganic crystals, including clays, layered double hydroxides, zeolites, cement phases, etc.[5,14,15]

Bulk crystal properties (lattice parameters, density, basal spacing, and bond distances) of various clay structures obtained from ClayFF were found to agree very well with experimental data.[1] The cleavage of the layered clay structure to expose the basal surface of a model clay platelet does not involve any bond breaking, logically enabling direct simulations of basal interfaces using the FF parameters developed to reproduce the bulk structure.[5] In contrast, cleavage of the structurally complex crystal edge surfaces leaves dangling bonds. As a consequence, models of neutral surfaces are obtained through nondissociative and dissociative H_2O sorption, otherwise known as physisorption and chemisorption of water at the surface, respectively. However, real clay platelets in nature have finite sizes, their surface charge depends on pH,[16−18] and many important physical-chemical processes occur predominantly at their edges or are specific to their edges. Indeed, pH-dependent mineral-water reactive processes occur at the edges, such as flocculation,[19,20] crystal growth, and dissolution,[21−25] as well as physical and chemical sorption.[26−35] Because of such a complexity, there is no reason to believe *a priori* that the FF parameters fitted to reproduce bulk crystal structures will be directly applicable to edge surfaces, even if a few simulations report attempts to model edge surfaces with ClayFF.[36−46]

Two recent studies reported direct comparisons between the results of edge surface modeling of pyrophyllite using ClayFF and DFT calculations with the GGA approximation. Martins et al.[44] found deviations of ClayFF with respect to the DFT results ranging from 3 to 30% in terms of surface energies of various edge cleavages and terminations. However, neither the

presence of interfacial water nor dynamical effects were accounted for in the comparison. Newton and Sposito[45] compared metal−O (M−O) distances at the hydrated clay edge derived from classical MD using ClayFF with DFT calculations[47] and found an underestimation of Si−O distances by 2−5% and an overestimation of Al−O distances by 1−5%. To our knowledge, no comparison between the results of classical (ClayFF) and quantum chemical calculations in terms of the structure and hydrogen bonding at the hydrated edge surface has yet been made.

Yu et al.[48] observed at moderate temperatures an unrealistic thermodynamic instability of the $(1\bar{1}0)$ edge surface of hydrotalcite, $Mg_6Al_2(OH)_{16}CO_3 \cdot 4H_2O$, simulated with ClayFF. They proposed to modify the original parametrization by a readjustment of partial atomic charges on the basis of comparison with their DFT calculations and by adding to ClayFF a new bending term for the Mg−O−H group. These modifications produced a better agreement with the DFT results in terms of surface energy for the systems of interest. Following this approach, Zeitler et al.[49] parametrized the Mg−O−H bending term using as models the bulk crystal and the basal and edge surfaces of brucite, $Mg(OH)_2$. They obtained a very good agreement with DFT (GGA) results for the Mg−O−H angle distributions and the vibrational density of states.

The objective of the present work is to re-evaluate the Mg−O−H bending term parametrization in application to hydrated edge surfaces of brucite and to systematically extend this approach to the Al−O−H bending term parametrization using the bulk crystal and the hydrated basal and edge surfaces of gibbsite, $Al(OH)_3$. In addition, we provide a detailed comparison of the structural and dynamic properties of hydrated brucite and gibbsite edge surfaces, derived from classical molecular dynamics (C-MD) simulations using the original ClayFF (ClayFF-orig), the modified ClayFF of the present work (ClayFF-MOH), and DFT molecular dynamics (DFT-MD) simulations in terms of metal−O−H angular distributions, hydroxyl group orientations, and the topology of the intersurface and surface water H-bonding networks formed at various surfaces. With the octahedral structures of brucite and gibbsite representing the principal backbones of many clay minerals, our results will lead to a greatly improved classical FF description of clay particle edges.

■ STRUCTURAL MODELS

Brucite. The structure of brucite, the only existing polymorph of magnesium hydroxide, $Mg(OH)_2$, consists of stacking layers built up by edge-sharing $Mg(OH)_6$ octahedra. Following the work of Zeitler et al.,[49] the bulk crystal, its hydrated basal surface, and $(1\bar{1}0)$ edge surface are considered here. The initial bulk structural model of brucite was based on the experimental X-ray diffraction data, which provides unit cell parameters of $3.15 \times 3.15 \times 4.77$ Å^3, $\alpha = \beta = 90°$, $\gamma = 120°$ trigonal symmetry.[50] To facilitate the analysis, the bulk cell was orthogonalized by redefining the **a** and **b** lattice vectors into **a*** = **a** − **b** and **b*** = **a** + **b**, resulting in a $5.46 \times 3.15 \times 4.77$ Å^3 orthorhombic cell of twice the volume of the unit cell, used as a basis for constructing the simulation supercells. The supercells were built by repeating the unit cells in all three special directions, with two different sizes: small supercells intended for the parametrization stage and DFT-MD runs and large supercells for the classical MD runs. A $2 \times 3 \times 2$ supercell was used for the small bulk model and the basal surface models. In
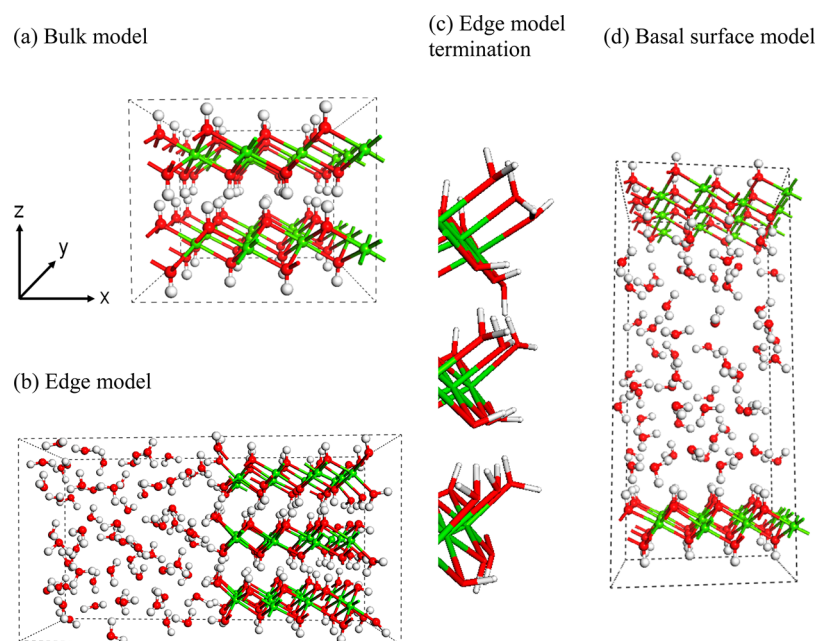
(a) Bulk model   (c) Edge model termination   (d) Basal surface model

(b) Edge model

Figure 1. Brucite small models. (a) Bulk model obtained by DFT geometry optimization; (b–d) DFT-MD snapshots. The models are oriented according to the coordinate system shown in (a). H_2O molecules not coordinated to Mg atoms are hidden in (c) for clarity.

(a) Bulk model   (c) Edge model termination   (d) Basal surface model

(b) Edge model

(e) Hydroxyl groups: xz plane

op3   op1   ip1   ip3   op2   ip2
ip2   op2   ip3   ip1   op1   op3

(f) Hydroxyl groups : xy plane

OH_{op3}
OH_{ip3} OH_{ip2}
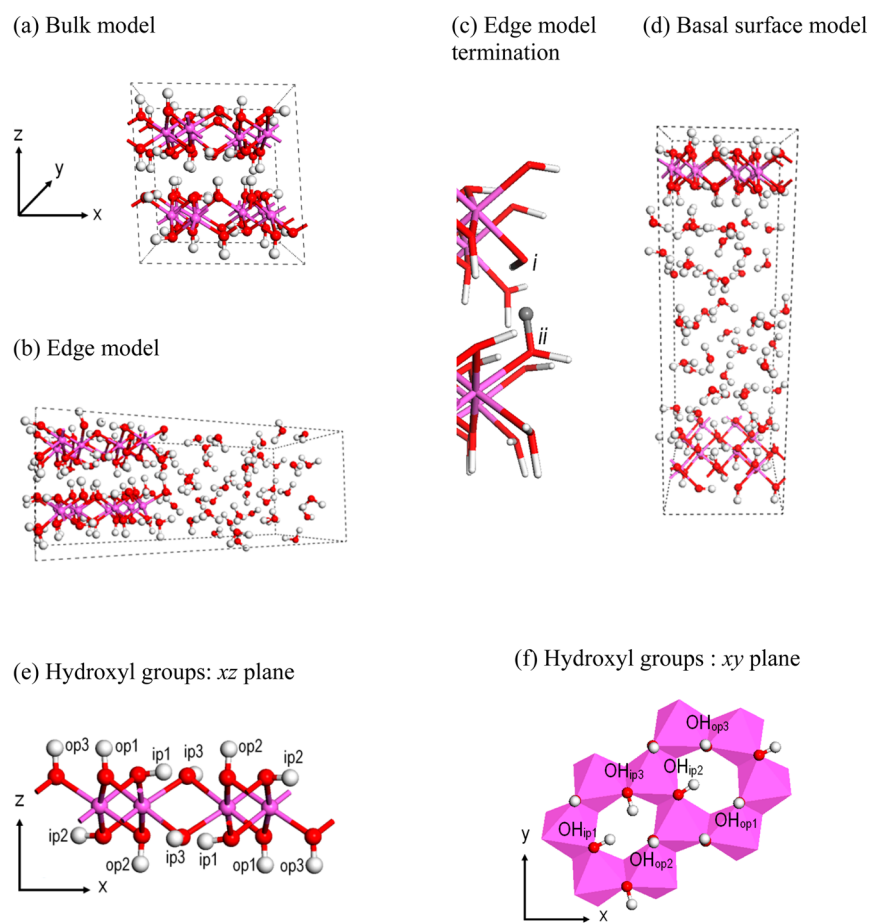OH_{ip1} OH_{op1}
OH_{op2}

Figure 2. Gibbsite small models and hydroxyl groups types. (a) Bulk model obtained by DFT geometry optimization. (b–d) DFT-MD snapshots. The models are oriented according to the coordinate system shown in (a). H_2O molecules not coordinated to Al atoms are hidden in (c) for clarity. The proton in gray was bonded to the atom Oi at $t = t_0$ and was transferred to the atom Oii during the DFT-MD run. The six types of hydroxyl groups oriented in the basal plane (OH_{ip}, in-plane) and out of the basal plane (OH_{op}, out-of-plane) are shown in (e) and (f) for the structures obtained by DFT geometry optimizations.

Table 1. Energies of Desorption at 0 K in Vacuum of a Water Molecule from the Brucite and Gibbsite Edge Surfaces Using DFT Calculations (kcal mol^{-1})[a]

	brucite (1$\bar{1}$0) edge	gibbsite (010) edge	
model A	18 Mg(OH)(OH$_2$)[b]	8 Al(OH)(OH$_2$)[b]	7 Al(OH)(OH$_2$) 1 Al(OH$_2$)(OH$_2$)
model B	17 Mg(OH)(OH$_2$) 1 Mg(OH)	7 Al(OH)(OH$_2$) 1 Al(OH)	7 Al(OH)(OH$_2$) 1 Al(OH$_2$)
$E_B + E_{H_2O} - E_A$	25.9	41.9	20.0

[a]Model B was obtained from model A by removing one of the metal-coordinated OH$_2$ groups. Models were relaxed with a short 3 ps NVT-ensemble MD run at T = 350 K followed by geometry optimizations. Energies in kcal mol^{-1}. E_{H_2O} is the energy of an isolated water molecule. [b]Models used in subsequent DFT calculations.

our test calculations, a brucite edge model with two layers produced excessively ordered interfacial water structure at T = 300 K, therefore a larger 2 × 3 × 3 supercell was subsequently used.

Gibbsite. The structure of gibbsite, the most stable polymorph of aluminum hydroxide, Al(OH)$_3$,[51−53] is formed by stacking layers built up by edge-sharing Al(OH)$_6$ octahedra. The initial bulk model of gibbsite was based on experimental neutron diffraction data, which provides unit cell parameters of 8.68 × 5.08 × 9.74 Å^3, $\alpha = \gamma = 90°$, $\beta = 94.54°$ monoclinic symmetry.[54] As proven experimentally[55,56] and confirmed theoretically,[51] gibbsite hydroxyl groups adopt two different orientations in the bulk: in the (001) plane (OH$_{ip}$) and along the [001] direction (OH$_{op}$). Among the possible edge surfaces, the (100) gibbsite surface, which is the one observed experimentally,[57] was studied here in addition to the bulk crystal and basal surfaces. The gibbsite supercells consisted of 1 × 2 × 1 and 3 × 5 × 3 crystallographic unit cells, respectively, for small and large structural models, and a 2 × 4 × 2 supercell was used for the DFT cell optimization.

Crystal Cleavage and Edge Termination. The basal and edge cleavages of the two bulk metal hydroxides produce two symmetric surfaces (Figures 1 and 2). As a consequence, the properties of the two surfaces are statistically equivalent. The brucite (1$\bar{1}$0) edge cleavage results in 2 broken Mg−O bonds per unit cell, resulting in 1 Mg atom coordinated to 5 OH groups instead of 6 OH groups in the bulk and 1 OH group coordinated to 2 Mg atoms instead of 3 Mg atoms in the bulk. The gibbsite (100) edge cleavage results in 3 broken Al−O bonds per unit cell, leaving 2 Al atoms each coordinated to 5 OH groups (instead of 6 OH groups in the bulk) and 1 OH group coordinated to 1 Al atom instead of 2 Al atoms in the bulk. To keep the mineral slab charge-neutral, the dangling bonds were satisfied by chemisorption or physisorption of water molecules.

We determined the energies of desorption of a single H$_2$O molecule from a Mg(OH)(OH$_2$) brucite edge site and from a Al(OH)(OH$_2$) gibbsite edge site to be +25.9 and +41.9 kcal mol^{-1}, respectively (Table 1). Liu et al.[58] calculated the free energy of desorption of one water molecule from a Al(OH$_2$)(OH$_2$) site, the protonated form of Al(OH)(OH$_2$), to liquid water at T = 300 K to be +10 kcal mol^{-1}. The value of the energy of the OH$_2$ desorption at 0 K for our dry gibbsite edge surface is +20.0 kcal mol^{-1} (Table 1). The difference is presumably due to the stabilizing interactions of a water molecule in liquid water and to all the entropic effects.

By comparing calculated energies of desorption between the vacuum and hydrated systems, and under a reasonable assumption that the effects of hydration and temperature have the same order of magnitude for all of these surfaces, we can safely predict that the free energy of desorption of one

water molecule from a brucite or gibbsite M(OH)(OH$_2$) site for a hydrated surface at 300 K is at least +10 kcal mol^{-1}, which justifies the termination of all the edge surfaces by one OH group and one OH$_2$ group at ambient temperature.

■ METHODS

DFT. Periodic DFT calculations used the generalized gradient approximation (GGA) with the PW91 functional, for consistency with the previous parametrizations.[1,49] The PW91 results agree well with experimental data in terms of the brucite cell parameters, fractional cell coordinates (relative errors of 1.1% and 1.4%, respectively), and vibrational frequencies of the crystals (within 10 cm^{-1}).[59,60] A comparison of the cell parameters and M−O bond lengths between the dispersion-corrected[61] PW91 results and experimental data for four clay minerals containing brucite- or gibbsite-like sheets shows only differences smaller than 0.5% and 1.0%, respectively.[62]

It is known that the simulation results with GGA functionals PW91 and PBE (essentially, a simplified version of PW91[63]) are very close in terms of the bulk properties of clay minerals[62] and bulk water structure.[64] It is also known that PW91 and PBE functionals produce overstructured bulk water, which is especially apparent when considering the height of the first peak of the radial distribution function $g_{OO}(r)$, and Grimme et al. dispersion corrections[61,65] do not significantly improve on this aspect.[66,67] In our DFT calculations, we used the DFT-D3 correction of Grimme et al.[65] The Gaussian and plane waves (GPW) scheme[68] was used here with a split-valence double-ζ basis set using a single set of polarization functions,[69] Goedecker-Tetter-Hutter pseudopotentials,[70] and a plane wave cutoff of 350 Ry for the density grid. Together with the cutoff, additional GPW settings (relative cutoff, SCF convergence criterion, and precision in the calculation of the Kohn−Sham matrix) enabled a small error in the calculated forces ($<10^{-4}$).

In DFT calculations the wave function was sampled at the Γ point, which allowed for a reasonable accuracy when the sizes of the mineral models are considered. For the parametrization calculations using small models, at least 15 Å of vacuum was added to all surface models to ensure the interaction of the platelet with its periodic image was negligible. For the MD simulations, a water slab was added instead to the platelet with respective widths of 15 and 30 Å for small and large structural models. The CP2K software[68] was used for all DFT calculations.

Force Field Parameters. All FF parameters except for the M−O−H bending terms are presented in Table 2. Nonbonded parameters were taken from the original ClayFF parametrization.[1] The original harmonic O−H-bond terms for the metal hydroxyl groups were replaced here with a more accurate Morse potential.[71] Water molecules, including the OH$_2$ groups

Table 2. Force Field Parameters

nonbonded[a]: $E_{nonbonded} = \frac{q_i q_j}{4\pi\epsilon_0 r} + 4\epsilon_{ij}\left[\left(\frac{\sigma_{ij}}{r}\right)^{12} - \left(\frac{\sigma_{ij}}{r}\right)^6\right]$				
species	symbol	q (e)	ϵ (kcal mol^{-1})	σ (Å)
hydroxide Mg	mgh	1.0500	9.0298×10^{-7}	5.2643
octahedral Al	ao	1.5750	1.3298×10^{-6}	4.2718
hydroxyl O	oh	−0.9500	0.1554	3.1655
hydroxyl H	ho	0.4250	0.000	0.0000
water O	o*	−0.8200	0.1554	3.1655
water H	h*	0.4100	0.000	0.0000
$E_{Morse}^{bond} = D_0[1 - e^{-\alpha(r-r_0)}]^2$				
bond	D_0 (kcal mol^{-1})		α (Å^{-1})	r_0 (Å)
oh−ho[b]	132.2491		2.1350	0.9572
$E_{quadratic}^{bond} = k(r - r_0)^2$				
bond	k (kcal mol^{-1} Å^{-2})			r_0 (Å)
o*−h*[71]	554.13			1.0000
$E_{quadratic}^{angle} = k(r - r_0)^2$				
angle	k (kcal mol^{-1} rad^{-2})			θ_0 (deg)
h*−o*−h*[1,73]	45.770			109.47

[a]Parameters of Cygan et al.;[1] $\sigma_{\alpha\beta} = 1/2\,(\sigma_\alpha\sigma_\beta)$ and $\epsilon_{\alpha\beta} = (\epsilon_\alpha\epsilon_\beta)^{1/2}$. [b]Two different sets were parametrized by Greathouse et al. for dioctahedral and trioctahedral clays,[71] and the set for trioctahedral clays was found to be optimal here.

attached to the M atoms, are described by the SPC model[72] with O−H bond stretching and H−O−H angle bending terms.[73] Because of the potential desorption of OH$_2$ groups, the M−O−H bending term is only applied to OH groups.

Parameterization of the Metal−O−H Bending Term. The bending term to be parametrized has the form of $E_{bend} = k\,(\theta - \theta_0)^2$, where θ is the ∠MOH angle. Its parametrization consisted of finding the values of the force constant k and the equilibrium angle θ_0, which minimized the differences between the DFT and classical ClayFF-MOH results. In the current work the following approach was used to define the optimization criteria and to determine the bending term parameters that minimize their values. (i) Using DFT, Γ-point vibrational modes were calculated after a local geometry optimization. (ii) Using ClayFF−MOH, a local geometry optimization was performed starting from the DFT-optimized structure, followed by the calculation of Γ-point vibrational modes. The geometry optimization and the calculation of vibrational modes were performed with the GULP software[74] for every value of θ_0 within the 90−130° range ($\delta\theta = 1°$), and for every value of k within the 0−40 kcal mol^{-1} rad^{-2} range ($\delta k = 1$ kcal mol^{-1} rad^{-2}), while all other ClayFF parameters were kept fixed. (iii) From the final structures and vibrational normal modes obtained for every pair of parameters (θ_0, k), absolute differences between DFT- and ClayFF-MOH-derived properties were calculated, in terms of wavenumbers and in terms of O−H orientations. The procedure is further detailed in the Supporting Information.

Finally, the model surfaces used in the static calculations were dry (basal surface) or hydrated by only one water layer (edge surface). Whereas the consideration of energy minima at $T = 0$ K for bulk solids is acceptable, the surface OH groups and the effect of the presence of liquid water on the surface create disorder, thus additional entropic effects. Therefore, the values of the parameters derived from the static calculations are informative but may not be necessarily optimal when

thermodynamic effects are included. In the simulations, a few other sets of (θ_0, k) values were also tested along with the optimal ones.

Molecular Dynamics. Molecular dynamics (MD) simulations were performed at $T = 300$ K using a time step of 0.5 fs, ensuring good sampling of the dynamics of hydrogen (H) atoms. Born−Oppenheimer molecular dynamics combined with DFT using the GGA approximation (DFT-MD) were used in the simulations of the small structural models, and implemented with the CP2K software.[68] DFT-MD simulations at a temperature higher than $T = 300$ K could limit the tendency to form overstructured liquid water at $T = 300$ K by the PW91 and PBE functionals,[67,75] but the mineral platelet and specifically the surface hydroxyl groups would obviously be also affected by this increase in temperature, which is problematic here since we intend to directly compare the results of DFT-MD and C-MD simulations. The values of the GPW-related settings allowed for a good conservation of the constant of motion (drift smaller than 5×10^{-7} Ha ps^{-1} per atom). C-MD simulations using ClayFF with and without the M−O−H bending term were used to simulate both the small and the large cells of brucite and gibbsite, using the LAMMPS software.[76]

The lattice dimensions, and the β angle for monoclinic cells, of the large bulk cells were relaxed using NPT-ensemble C-MD simulations at $P = 1$ bar during 250 ps using the Nose-Hoover chains thermostat[77] and the Parrinello−Rahman barostat.[78] The small bulk cells were relaxed using DFT cell optimizations. For small surface models, the dimension perpendicular to the surface was relaxed by performing NPT-ensemble DFT-MD for 10 ps. For large basal surface models, the dimension perpendicular to the surface was relaxed by performing NPT-ensemble DFT-MD for 100 ps. For large edge models, a NVT-ensemble MD pre-equilibration run was first performed at $T = 200$ K for 100 ps to avoid initial layer distortion, desorption of OH groups, and excessive desorption of OH$_2$ groups, which was otherwise observed with classical simulations when a nonequilibrated edge model was directly subjected to a temperature of $T = 300$ K. Then the dimension of the edge model cell perpendicular to the surface was relaxed by performing NPT-ensemble C-MD for 1 ns, during which the coordination state of the metal atoms by OH$_2$ groups reached equilibrium. The equilibrium average cell dimensions and angles were then assigned to the cells for the following simulations. After a final equilibration of atomic positions and velocities by performing NVT-ensemble MD for 10 ps (DFT-MD) and 100 ps (C-MD), production runs were performed in the NVE ensemble for 100 ps (C-MD) and 40 ps (DFT-MD), collecting atomic positions and velocities every 1 fs. The trajectories of the NVE-ensemble simulations were initiated from the last configurations of the NVT-ensemble MD trajectories with the velocities rescaled at $T = 300$ K. During the course of the NVE-ensemble simulations, the effective average temperature remained constant, taking a value between 295 and 305 K. The DFT-MD simulations of gibbsite edge surfaces, subject to proton hopping, were extended up to 100 ps.

To account for a possibility of dehydroxylation, Zeitler et al.[49] proposed a "nonbonded three-body" M−O−H bending term, which was derived for implementation within LAMMPS. It was switched on only if certain minimum M−O and M−H distance criteria were satisfied. In the current work, we applied the same term to all M−O−H groups unconditionally, based

Table 3. Brucite and Gibbsite Lattice Parameters Rescaled to the Unit Cell Using DFT, ClayFF-orig, and ClayFF-MOH[a]

	exp.[50]	DFT	ClayFF			
			orig	MOH $\theta_0 = 120°$	MOH $\theta_0 = 110°$	MOH $\theta_0 = 100°$
Brucite[b]						
supercell	−	$2 \times 4 \times 3^c$	$4 \times 7 \times 5^c$			
a	3.15	3.20	3.27	3.27	3.27	3.33
c	4.77	4.62	4.74	4.74	4.74	4.69
V	41.00	40.90	43.78	43.80	43.76	45.07
diff. wrt. exp.[d]	−	2.26	2.39	2.37	2.35	4.00
diff. wrt. DFT[d]	−	−	2.37	2.39	2.36	3.11

	exp.[54]	DFT	ClayFF			
			orig	MOH $\theta_0 = 116°$	MOH $\theta_0 = 110°$	MOH $\theta_0 = 100°$
Gibbsite						
supercell	−	$2 \times 4 \times 2$	$3 \times 5 \times 3$			
a	8.68	8.66	8.87	8.84	8.83	8.85
b	5.08	5.05	5.13	5.16	5.17	5.19
c	9.74	9.56	9.81	9.84	9.83	9.79
β	94.5	94.1	100.6	93.8	91.5	97.9
V	428.0	417.2	439.0	447.9	448.6	445.4
interlayer spacing	4.85	4.77	4.82	4.91	4.91	4.85
diff. wrt. exp.[d]	−	1.02	5.42	1.73	3.29	3.66
diff. wrt. DFT[d]	−	−	6.10	2.45	3.46	4.38

[a]Lengths are in Å, angles in degrees, volumes in Å^3. Average NPT MD (300 K, 1 bar) values at equilibrium for classical calculations, cell optimization for DFT. [b]The brucite interlayer spacing is equal to c/2. [c]Supercell with respect to the orthorhombic cell built from the trigonal unit cell according to $a' = a - b$ and $b' = a + b$. For theoretical results, the statistical uncertainty is lower than the given decimal precision (i.e., inferior to 0.01 Å for lengths and inferior to 0.1° for angles). [d]In %; cf. eq 1.

on the initial optimized structures. Indeed, even with a selection of the optimal cutoff criteria, the succession of activations and deactivations of the term often led to a drift of the total energy, apparent in NVE-ensemble simulations. Of course, the permanent activation of the term is only valid if there is no actual dehydroxylation in the course of the simulation run, which was the case for gibbsite and brucite edge surfaces at T = 300 K.

The average bulk lattice parameters from MD runs were compared with experimental values. To evaluate the effect of the bending term on the intrinsic structure and dynamics of hydroxyl groups, distributions of the ∠MOH angle and the O−H bond orientation were calculated.

■ RESULTS AND DISCUSSION

Static Calculations. The proposed approach for the parametrization was first applied to brucite models (bulk crystal and basal surface) in order to compare the results with the earlier calculations of Zeitler et al.[49] Subsequently, the method was used for the edge surface of brucite, and the bulk crystal, the dry basal surface, and the edge surface of gibbsite.

To estimate the optimal values of the equilibrium angle θ_0 and the force constant k, absolute differences between DFT and ClayFF-MOH results were plotted against the two parameters in the form of heat maps, where θ_0 and k are the two dimensions of the map and the differences are represented by a color range. They are presented in section I of Figures S1−S6. Globally, the optimal areas are large enough to allow reasonable compromises between different structural models in the selection of the final parameters and for an integer precision in the selected values of the parameters to be sufficient.

A θ_0 value of 110° is a good compromise for all the gibbsite models, together with a force constant of k = 15 kcal mol^{-1} (Figures S1−S3). The experimental ∠AlOH value in the bulk is

unknown, since the structural studies of the gibbsite bulk crystal were limited to X-ray diffraction, a technique that does not precisely locate the H atoms. From our DFT-MD studies, the average ∠AlOH in the bulk is 116°, therefore the performance of ClayFF-MOH with $\theta_{0,\text{AlOH}} = 110°$ was compared to that of ClayFF-MOH with $\theta_{0,\text{AlOH}} = 116°$ in terms of the MD-derived structural properties.

As far as the brucite models are concerned, in terms of $\langle |\Delta\nu| \rangle$ (eq S2) the optimal force constant is clearly lower than the one for gibbsite (Figures S4−S6), the value k = 6 kcal mol^{-1} rad^{-2} being a reasonable choice for the Mg−O−H term. This value is in agreement with those found by Zeitler et al.[49] (5.08 and 5.81 kcal mol^{-1} rad^{-2} for the bulk and the basal surface, respectively) and with their final retained value of 6.35 kcal mol^{-1} rad^{-2}, originally selected by Yu et al.[48] The equilibrium angle can be chosen the same as for the Al−O−H term (i.e. $\theta_{0,\text{MgOH}} = \theta_{0,\text{AlOH}}$ = 110°). The performance of the ClayFF-MOH parametrization with $\theta_{0,\text{MgOH}} = 110°$ and $\theta_{0,\text{MgOH}} = 120°$ was compared in terms of MD-derived structural properties. The latter value was used by Zeitler et al.[49] and Yu et al.[48] because it is the value of ∠MgOH obtained by neutron diffraction.[79]

Since the value of $\theta_0 = 100°$ is in the range of acceptability for all brucite and gibbsite models, its performance was also tested alongside the aforementioned θ_0 values. In the following C-MD results obtained with ClayFF-MOH, the values of the force constants are fixed ($k_{\text{MgOH}} = 6$ kcal mol^{-1} rad^{-2}, $k_{\text{AlOH}} = 15$ kcal mol^{-1} rad^{-2}) and "ClayFF-MOH-X°" stands for "ClayFF-MOH with $\theta_0 = X°$".

Lattice Parameters. The difference of lattice parameters derived from C-MD and DFT values with respect to the experimental values, and the difference of lattice parameters derived from C-MD with respect to the DFT values, is based on the lattice vectors (u_1, u_2, u_3):
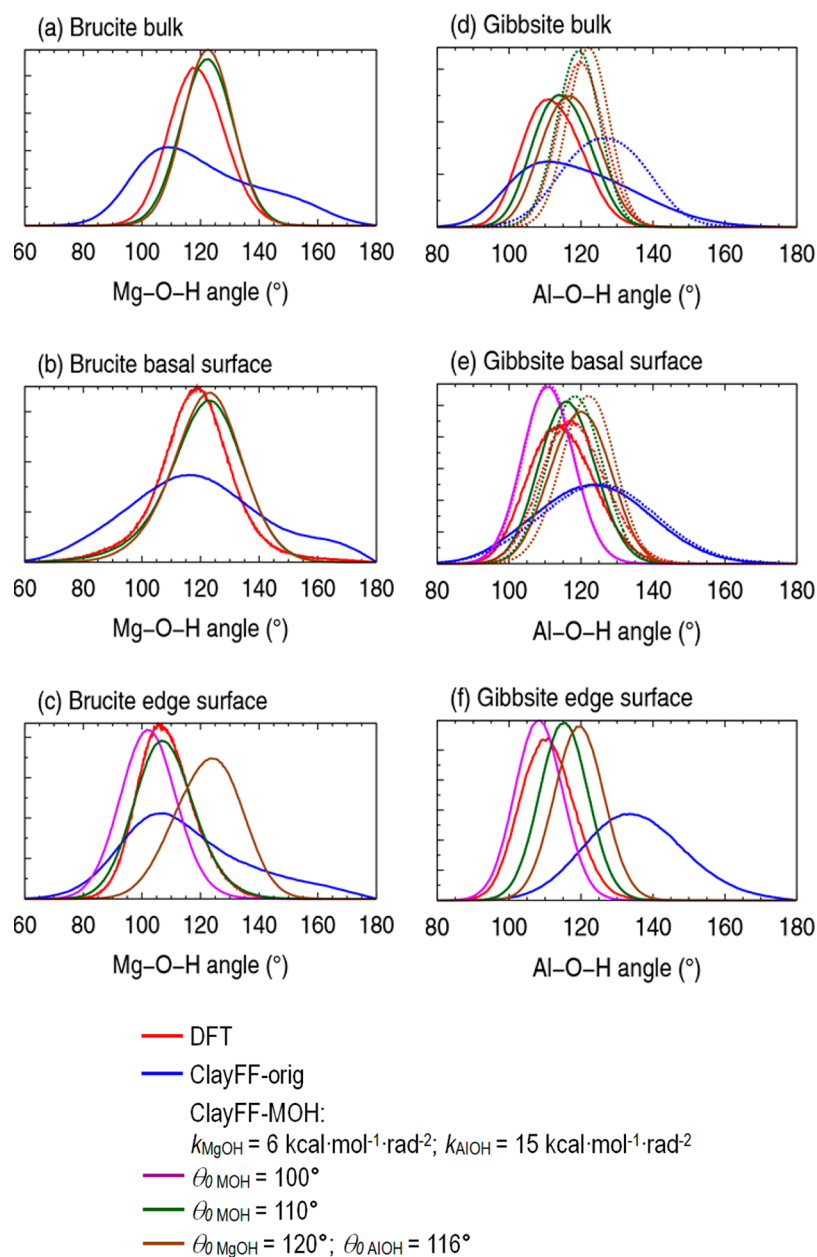
Figure 3. Metal−O−H angle distributions for the brucite and gibbsite models. (d and e) OH_{ip} and OH_{op} groups are represented by a solid and a dashed line, respectively.

$$\frac{\sum_{i=1}^{3} \| \mathbf{u}_i - \mathbf{u}_{iref} \|}{\sum_{i=1}^{3} \| \mathbf{u}_{iref} \|}, \text{ with } \| \mathbf{u}_1 \| = a, \| \mathbf{u}_2 \| = b, \| \mathbf{u}_3 \| = c \quad (1)$$

As far as brucite is concerned, Zeitler et al.[49] observed that the bending term did not affect lattice parameters. From our NPT-ensemble simulations, the Mg−O−H bending term did not decrease the error on the lattice parameters: ClayFF-orig, ClayFF-MOH-110°, ClayFF-MOH-120° all lead to a reasonable 2.35−2.39% error with respect to experimental values, while ClayFF-MOH-100° results in a higher 4.00% error (Table 3).

The influence of the Al−O−H bending term on the gibbsite lattice parameters is shown in Table 3, along with the DFT results and experimental values. The respective values of a, b, and c are not significantly influenced by the parametrization;

however, the value of θ_0 largely impacts the β angle. ClayFF-orig overestimates β by 5.9° with $\beta = 100.6°$ instead of the experimental value $\beta = 94.5°$ (Table 3). When applying the MOH term, the β angles are 93.8°, 91.5°, and 97.9°, respectively, for $\theta_0 = 116°$, $\theta_0 = 110°$, and $\theta_0 = 100°$. The total error with respect to experiment (Table 3) reduces from 5.42% (ClayFF-orig) to 3.66% ($\theta_0 = 100°$), 3.29% ($\theta_0 = 110°$), and 1.73% ($\theta_0 = 116°$).

Proton Transfer. While no proton exchange was observed between surface hydroxyl groups and interfacial water molecules, multiple proton transfer events occurred at the edge surfaces of gibbsite and brucite in DFT simulations between an OH_2 group and a hydroxyl group of the neighboring mineral layers. Such events were not reported by the previous DFT-MD study of the gibbsite edge surface[58] probably because the repartition of the protons between edge sites, different from ours, did not favor proton hopping. Proton

transfer is clearly enabled by physical interactions with interfacial water molecules since it was not observed in our test DFT-MD runs of the dry edge surfaces. The vast majority of these proton transfer events were very short incursions, typically on the order of magnitude of the O–H stretching vibration period, of one H_{OH2} atom on the neighboring O_{OH} atom, after which the proton returned back to the original O_{OH2} atom.

On the gibbsite edge surfaces, ten or less of these proton hops were "successful", in that the proton stayed on the neighboring O for more than 1 ps, while no successful hops occurred on the brucite edge surface. Proton hopping is illustrated via the time evolution of the distance between the protons and their two closest O atoms of the surface in Figure S7. A snapshot from the DFT-MD simulation of the gibbsite edge surface is shown in Figure 2c, illustrating the edge termination after a proton hopping event. To calculate MD-derived structural properties, for each configuration belonging to the DFT-MD trajectory, OH and OH_2 groups were identified based on a O–H distance cutoff of 1.2 Å, the optimal value determined from Figure S7.

Metal–O–H Angle and O–H Bond Orientation of Surface Hydroxyl Groups. Since the new M–O–H bending term is applied to angles, the metal–O–H angle (∠MOH) distribution is the most immediate structural property to be influenced by its activation. The ClayFF-orig parametrization greatly overestimates, typically by a factor of 2, the ∠MOH standard deviation compared to the DFT results (Figure 3). As a general trend, the introduction of the M–O–H bending term systematically improves over the ClayFF-orig performance by reducing this standard deviation. As a result, the full widths at half-maximum (FWHM) of the ClayFF-MOH distributions do not differ more than 3.0° from the respective DFT results.

Three-dimensional plots illustrate the probability, represented by a color range, to find two of the three components of the O–H bond vector (Figures 4 and 5). For the bulk and basal surface cells, the x and y components of the O–H vector are represented, with x and y defining the basal plane. As far as the gibbsite and brucite edge surfaces are concerned, the most relevant O–H components are x and z, x being the direction perpendicular to the edge surface and z being the direction perpendicular to the basal plane (Figures 1 and 2). Due to the similarity between ClayFF-MOH-100°, with $\theta_0 = 110°$ and with $\theta_0 = 120°$ (brucite) or $\theta_0 = 116°$ (gibbsite) in terms of the O–H orientational distributions, only the distributions obtained by ClayFF-MOH-110° are shown in Figures 4 and 5 alongside the DFT and ClayFF-orig results. Additionally, the density profiles of the O and H atoms of the gibbsite and brucite edge hydroxyl groups are given in Figure S8.

As a consequence of the narrowing of all ∠MOH distributions, the orientations of all O–H bond vectors become more localized leading to a much better agreement with the DFT results. A strong and expected effect of the M–O–H bending term common to all surfaces is the reduction of the extent of the O–H orientational distributions, resulting in more focused spots.

Brucite Bulk and Basal Surface. It was proven by neutron diffraction[50,80,81] and confirmed later by static DFT calculations[82] that at high pressure, the brucite hydroxyl groups are not exactly oriented along the 3-fold [001] axis and that the deviation of the hydroxyl groups from this axis increases with pressure. Experiments did not clearly show if this deviation occurs at atmospheric pressure, but DFT simulations already
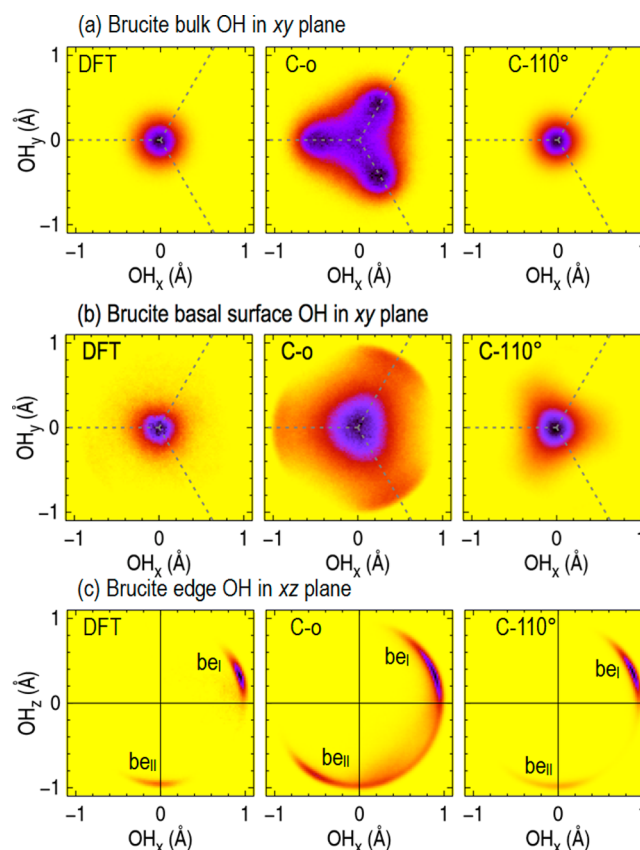

Figure 4. Orientation of brucite hydroxyl groups: distribution of the O–H bond vectors projected on the xy and xz crystallographic planes according to DFT (left), ClayFF-orig (center), and ClayFF-MOH-110° with $k = 6$ kcal mol^{-1} rad^{-2} (right) MD simulations. The basal and the edge planes are oriented, respectively, parallel to xy and yz (Figure 1, panels a and b). The color range from the lowest to the highest intensity is yellow, red, blue, and black. The projections of the O–Mg vectors on the xy plane are shown as gray dashed lines in (a) and (b). The regions of high intensity labeled "be$_x$" (brucite edge) are discussed in the text.

predicted that at $T = 300$ K and $P = 1$ bar, the most probable orientation of the brucite bulk OH groups is exactly along the [001] axis and the probability decreases when the distance r from the axis increases[83] with r defined as

$$r^2 = OH_x^2 + OH_y^2 \tag{2}$$

with OH_x and OH_y the components of the O–H bond vector along x and y directions, respectively. Our DFT-MD results confirm this preferred orientation of the bulk hydroxyl groups (Figure 4).

The distribution also peaks at $r = 0$ for the basal surface OH groups, but it is slightly more diffuse (Figure 4b). Accordingly, the standard deviation of ∠MgOH obtained from DFT-MD ranges from 9.6° for the bulk to 13.9° for the hydrated basal surface, as illustrated in the broadening of the distributions (Figure 3, panels a and b). The hydration alone explains this broadening, since the width of the dry basal surface distribution is identical to the bulk one.[49]

The distribution derived from the ClayFF-orig simulations incorrectly predicts some deviation of the O–H vector from the z axis in the bulk. Indeed, the three regions of highest intensity are away from the z axis (Figure 4a). This explains why the angle corresponding to the maximum of the ClayFF-
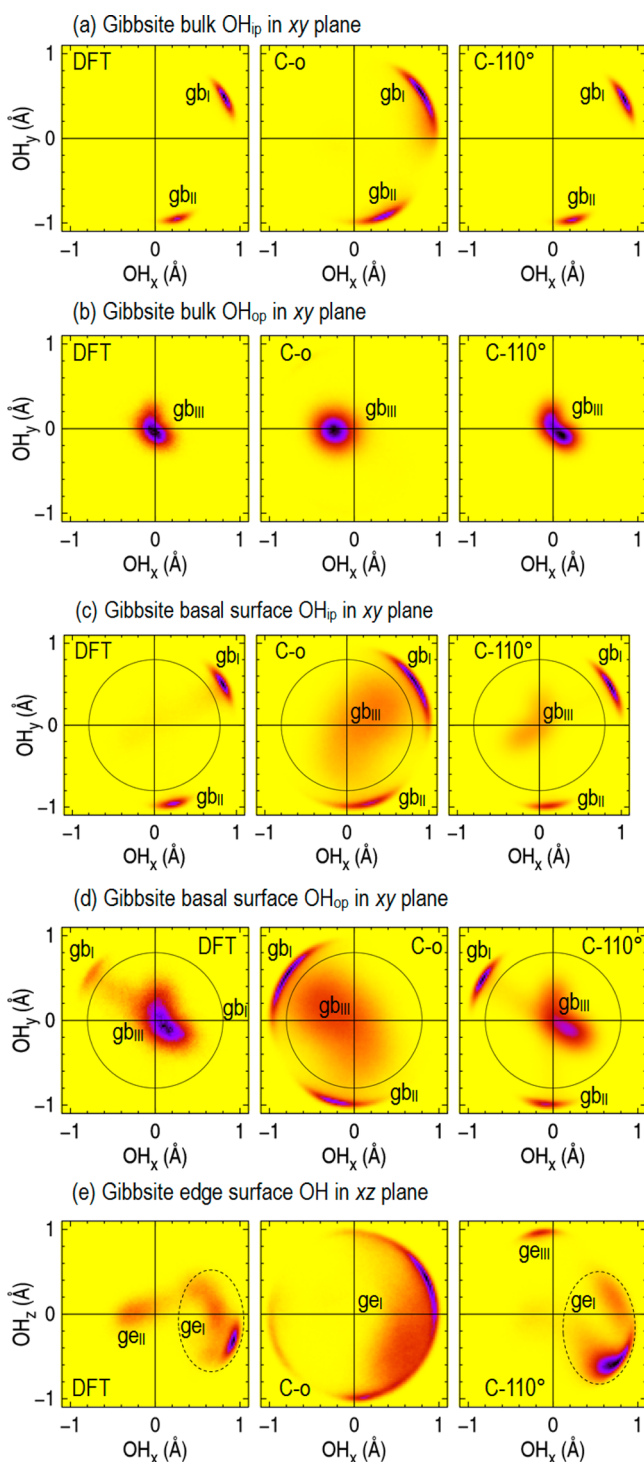
Figure 5. Orientation of gibbsite hydroxyl groups: distribution of the O−H vector projected on the *xy* and *xz* crystallographic planes according to DFT (left), ClayFF-orig (center), and ClayFF-MOH-110° with k = 15 kcal mol^{-1} rad^{-2} (right) MD simulations. The basal and edge planes are oriented, respectively, parallel to *xy* and *yz* (Figure 2, panels c and d). The color range from the lowest to the highest intensity is yellow, red, blue, and black. The circle with r = 0.8 Å represents the boundary between the "in-plane" and "out-of-plane" orientations of the hydroxyl groups for the calculation of the respective intensities. The regions of high intensity labeled "gb$_X$" (gibbsite bulk and basal surface) and "ge$_X$" (gibbsite edge) are discussed in the text.

orig ∠MgOH distribution, ∠MgOH^{max}, is only at 109.4°, compared to the higher 118.3° DFT value (Figure 3a).

However, for the basal surface hydroxyl groups ∠MgOH^{max} = 115.8°, closer to the 119.0° DFT value than in the bulk. This is consistent with the most probable orientation of the O−H groups belonging to the basal surface, which, contrary to the bulk, correctly coincides with the *z* axis (Figure 4b).

Brucite Edge Surface. The brucite edge model in the current work differs from the one of Zeitler et al.[49] due to the respective presence and absence of the OH$_2$ groups coordinated to edge Mg atoms, the latter form being less likely (Table 1). This translates into a strong difference in the DFT ∠MgOH angular distribution with ∠MgOH^{max} = 106.3° (Figure 3c), 20° lower than for the edge surface without OH$_2$ groups.[49] C-MD simulations with ClayFF-orig also result in ∠MgOH^{max} = 106.3°, and the ClayFF-MOH-120° parametrization, with ∠MgOH^{max} = 124.1°, do not result in the best match with the DFT distribution. However, using C-MD simulations with ClayFF-MOH-110° and ClayFF-MOH-100° result in ∠MgOH^{max} at +0.6° and at +4.8° from the value obtained by DFT-MD, respectively. The FWHM of the distributions obtained from ClayFF-MOH-110° (23.7°) and ClayFF-MOH-100° (22.2°) are close to the value obtained from DFT-MD (21.3°). The distribution of the O−H vector in the *xz* plane resulting from the DFT calculations (Figure 4c) peaks mostly along *x* in the "be$_I$" region, which represents 81% of the total intensity. This spot is also present in the C-MD-derived distributions where it accounts for approximately 37% in the case of ClayFF-orig and 56% in the case of ClayFF-MOH-110° models (Figure 4c). Additionally, contrary to the ClayFF-orig results, ClayFF-MOH-110° model leads to the formation of very distinct "be$_I$" and "be$_{II}$" spots, similar to the DFT-produced orientational distributions.

The Mg−O−H bending term restrains the O−H mobility along the *z* axis, which results in the most probable orientation at r = 0 in Figure 4a, similar to the DFT result but more tightly centered about the *z* axis.

Gibbsite Bulk. As proven experimentally,[55] gibbsite hydroxyl groups adopt two orientations in the bulk crystal (Figure 2) and can be sorted accordingly: the OH groups oriented almost entirely in the *xy* plane are called OH$_{ip}$ and the OH groups along the *z* direction are called OH$_{op}$. In the *xy* plane OH$_{ip}$ groups have two preferable orientations illustrated by the two spots labeled "gb$_I$" and "gb$_{II}$" in Figure 5a. Using the naming convention of Figure 2 (panels e and f), the spot "gb$_I$" corresponds to the OH$_{ip1}$ and OH$_{ip2}$ groups, and the spot "gb$_{II}$" corresponds to the OH$_{ip3}$ groups, as confirmed by the ratio between the two intensities which is exactly 2:1. C-MD simulations with ClayFF-orig and ClayFF-MOH-110° correctly locate the maxima of the "gb$_I$" and "gb$_{II}$" spots (Figure 5a) and their relative intensities, indicating that different OH$_{ip}$ groups keep their respective orientations during the C-MD run.

The addition of the M−O−H bending term in the case of the ClayFF-MOH-110° model reduces the extent of these spots to bring them very close to DFT results (Figure 5a). The OH$_{op}$ groups are oriented slightly away from the *z* axis with the ClayFF-orig model ("gb$_{III}$" spot in Figure 5b), but this is corrected in the ClayFF-MOH-110° model (Figure 5b). As shown in Figure 3d, DFT calculations predict that the ∠AlOH$_{op}$ distribution is narrower (FWHM = 15.1°) than the ∠AlOH$_{ip}$ distribution (FWHM = 20.0°). This could be explained by the topology of the local H-bonding network. Indeed, OH$_{op}$ groups donate H-bonds to the neighboring layer, which are much stronger than the intralayer H-bonds donated by OH$_{ip}$ groups to OH$_{op}$ groups. This also explains the

cohesion of the gibbsite layers.[55,56,84] The C-MD simulations with the ClayFF-MOH model result in the ∠AlOH angular distributions with FWHM much closer to the DFT results, with FWHM ≈19.3° for the OH_{ip} groups and FWHM ≈14.0° for the OH_{op} groups. The maxima are different for the ClayFF-MOH-110° and ClayFF-MOH-116° sets of parameters, since the $∠AlOH_{op}^{max}$ values differ from the DFT results by 3.2° and 6.0°, respectively, while the $∠AlOH_{op}^{max}$ values differ from their respective DFT results by 0.5° and 2.3°, respectively (Figure 3d).

Gibbsite Basal Surface. In the following, a basal surface hydroxyl group is considered "in-plane" if $r > 0.8$ Å, r being defined in eq 2. According to the DFT calculations, the orientations of the hydroxyl groups of the gibbsite basal surface are largely preserved, compared to the bulk, with most of the $O-H_{ip}$ vectors in the xy plane and most of the $O-H_{op}$ vectors along the z axis (Figure 5, panels c and d). However, the probability of the in-plane orientation is 84%, which means that a small fraction of the initially in-plane $O-H_{ip}$ groups switch their orientation to out-of-plane (the corresponding spot is hardly visible in Figure 5c). This is consistent with the ratio of intensities of the spots "gb_I" and "gb_{II}" equal to 1.75:1 instead of 2:1 in the bulk, which means that the reorientation to out-of-plane necessarily originates from the $O-H_{ip1}$ and $O-H_{ip2}$ groups. In addition, a fraction of originally in-plane $O-H_{ip}$ groups switch their orientation to out-of-plane. Indeed, in Figure 5d, the spot "gb_I" represents approximately 5% of the total intensity. The distributions for $∠AlOH_{ip}$ and $∠AlOH_{op}$ of the basal surface are much closer to each other (Figure 3e). According to DFT calculations, the values of $∠AlOH_{ip}^{max}$ and $∠AlOH_{op}^{max}$ are 113.9° and 116.9°, respectively, higher and lower than the corresponding bulk values, while their FWHM are 22.0 and 21.0°, respectively, both higher than the bulk values.

The smallest differences between the ClayFF-MOH and DFT results in terms of the ∠AlOH distributions for the basal surface are obtained by using the parametrization ClayFF-MOH-110°, for which $∠AlOH_{ip}^{max}$ and $∠AlOH_{op}^{max}$ values are only 2.2° and 1.5°, respectively, greater than their corresponding DFT values (Figure 3e). Similar to the bulk comparisons, the $∠AlOH_{ip}$ and $∠AlOH_{op}$ distributions obtained by using the ClayFF-MOH-116° model are shifted to higher angles (120° and 122°) than with $θ_0 = 110°$, and their FWHMs are similar. Using the ClayFF-MOH-100° model, the distributions for the two types of hydroxyl groups almost coincide; they are narrower (FWHM = 16.9°) and have $∠AlOH^{max} = 111.0°$, which is lower than the DFT value.

As far as the hydroxyl orientation is concerned, fewer OH_{ip} groups are oriented in the basal plane than with DFT results. Indeed, the application of the ClayFF-orig model results in a very large region "gb_{III}" spreading from $r = 0$ to $r ≈ 0.8$ Å and the probability of the in-plane orientation, above $r = 0.8$ Å according to our convention, is reduced to only 40% (Figure 5c), less than half of the DFT-derived probability. The application of the ClayFF-MOH-110° model leads to an improved 55% probability for the in-plane orientation (Figure 5c). The C-MD distribution of the $O-H_{op}$ vector in the xy plane shows two in-plane spots "gb_{II}" and "gb_{III}" (Figure 5d), whose total intensity is 33% with the ClayFF-orig model and 25% with the ClayFF-MOH-110° model (i.e., a little closer to the DFT results).

Gibbsite Edge Surface. All gibbsite edge ∠AlOH distributions are narrower than the ones for the basal surface (Figure

3f) due to hydroxyl groups involved in stronger H-bonds. The DFT-MD value of $∠AlOH^{max} = 110.4°$ has the closest C-MD counterpart of 108.4° corresponding to the ClayFF-MOH-100° model, while the values of $∠AlOH^{max}$ obtained with $θ_0 = 110°$ and $θ_0 = 116°$ are 115.5° and 119.6°, respectively. The FWHM obtained from DFT-MD and C-MD with ClayFF-MOH are all very similar and fall in a narrow angular range between 15.6° and 17.5°. The DFT calculations predict that the O−H vector in the xz plane is primarily oriented along x (Figure 5e); the main spot of the distribution "ge_I" ranges from $OH_x ≈ 0.3$ to $OH_x = 1.0$ Å, comprising 74% of the total intensity and reaches its maximum close to the x direction ($OH_x = 0.9$, $OH_z = -0.3$). The secondary lower intensity spot "ge_{II}" is located slightly away from the y axis. With the ClayFF-orig model, the distribution also has its maximum close to the x axis but extends over 180° and to $r ≈ 0.4$ Å (Figure 5e). At the same time, the improved ClayFF-MOH-110° model predicts a much more localized "ge_I" spot than with the ClayFF-orig model, comprising 80% of the total intensity of the distribution, close to the DFT results, and with a maximum at a slightly lower $O-H_z$ value than its DFT counterpart (Figure 5e). The remaining intensity essentially lies in the spot "ge_{III}" along the z axis, absent in the DFT distribution (Figure 5e).

Edge Surface: OH_2 Groups. *Metal−OH_2 Coordination.* In the MD configurations at $t = 0$, all metal atoms (Mg or Al) belonging to the edge surface are coordinated to four bulk hydroxyl groups and two surface groups: one hydroxyl group and one OH_2 group (Figures 1c and 2c). During DFT-MD and C-MD simulations alike, all hydroxyl groups remain attached to their respective metal (M) atoms during the entire simulation run. Desorption of OH_2 groups is unlikely, more so for the gibbsite edge as shown in Table 1. The M−OH_2 coordination number (CN) is given by the running coordination number (RCN) of the M−O_{OH2+w} pair at $r ≈ 3.0$ Å, corresponding to the minimum between the first and second peaks of the corresponding radial distribution function (RDF) (Figure 6). The first peak corresponds to OH_2 groups, and the second peak corresponds to the sum of the neighboring OH_2 groups and the H_2O molecules of the aqueous interface.

During the DFT-MD simulations, all adsorbed OH_2 groups remain connected to their original Al atoms, since the Al−OH_2 CN is 1.0 (Figure 6). For C-MD simulations using the ClayFF-orig model, only a portion of edge M atoms are coordinated to OH_2 groups, as indicated by the Mg−OH_2 and Al−OH_2 CN being equal to 0.74 and 0.38, respectively. In recent simulations of a montmorillonite edge model using ClayFF-orig, Newton et al.[46] also reported M−O CN lower than 1.0, with Mg−OH_2 CN of 0.72 and Al−OH_2 CN of 0.25 or 0.81, depending on the site. The brucite edge surface Mg−OH_2 coordination is 0.43, 0.93, and 0.98 for ClayFF-MOH with $θ_0 = 120°$, $θ_0 = 110°$, and $θ_0 = 100°$, respectively (Figure 6a), thus the Mg−OH_2 coordination is very sensitive to $θ_0$, and the optimal value is $θ_0 = 100°$. The CNs for the gibbsite edge surface Al−OH_2 groups are 0.95, 0.96, and 0.98 for ClayFF-MOH-116°, 110°, and 100°, respectively (Figure 6), thus merely activating an explicit Al−O−H bending term greatly improves the Al−OH_2 coordination by 0.6 units, compared to the DFT results, and this improvement is not very sensitive to $θ_0$.

Understandably, the inclusion of the M−O−H bending term does not significantly change the distance corresponding to the first peak of the M−O_{OH2+w} RDF maximum. For the brucite edge, it is located at 2.13 and 2.29−2.31 Å for DFT and the two ClayFF implementations, respectively, while for the gibbsite
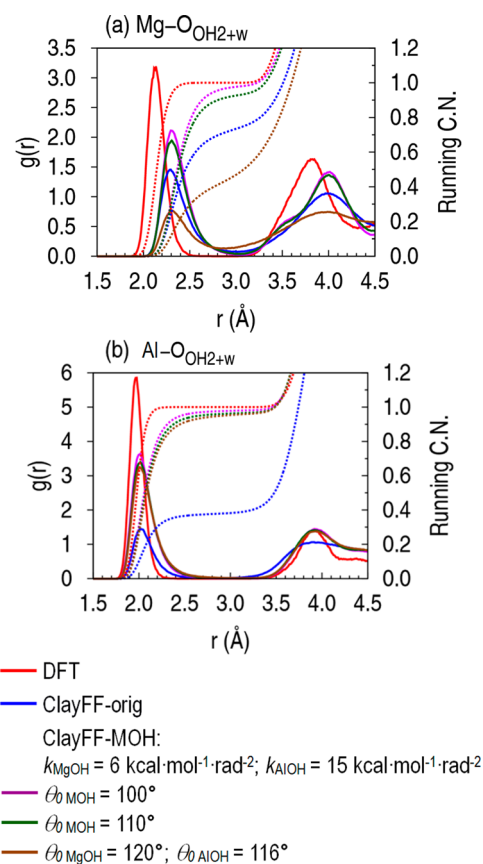
Figure 6. Radial distributions functions (solid lines) and running coordination numbers (dashed lines) for the M−O$_{OH2+w}$ pairs of the (a) brucite and (b) gibbsite edge surfaces.
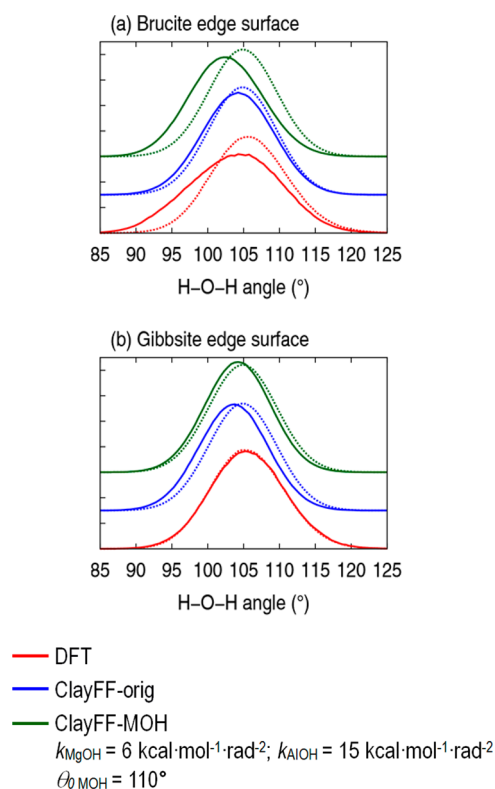

Figure 7. H−O−H angle distributions for the OH$_2$ groups (solid lines) on the edge surfaces of (a) brucite and (b) gibbsite. The distribution of the H−O−H angle of liquid water (dotted lines) is also given for comparison.

edge it is located at 1.97 and 2.01−2.03 Å for DFT and the two ClayFF implementations, respectively.

In the structural analysis, the distinction between the bound OH$_2$ groups and interfacial water molecules was based on the distance between the O atom and the closest M atom. If it was less than 3.0 Å, the species was treated as an OH$_2$ group, otherwise the species was considered as a water molecule of the interface.

For the gibbsite and brucite edge surfaces, as well as for the gibbsite basal surface, the performances of the ClayFF-MOH-100° and ClayFF-MOH-110° models are comparable, in terms of the surface ∠MOH angle distributions and the M−OH$_2$ coordination, and they produce better comparisons with the DFT results than those of the ClayFF-MOH-120° and ClayFF-MOH-116° models. Therefore, the optimum value of the equilibrium angle is selected as $\theta_{0,AlOH} = \theta_{0,MgOH} = 110°$ and from hereon the "ClayFF-MOH-110°" set of parameters is simply called "ClayFF-MOH".

H−O−H Angle. Given that the flexible SPC model was used not only to model water molecules but also the edge OH$_2$ groups, we need to evaluate the relevance of the H−O−H bending parameters, thus ∠HOH distributions of the OH$_2$ groups were determined for the brucite and gibbsite edges (Figure 7). The DFT-MD-derived ∠HOH distributions of the gibbsite edge OH$_2$ groups coincide with that of the interfacial water molecules (Figure 7b). DFT calculations correctly predict the mean liquid water ∠HOH angle to be 105.9°, agreeing with the experimental value of 106.1° ± 1.8°.[85] As far as the C-MD ∠HOH distributions are concerned, the ∠HOH^{max} values for

OH$_2$ groups are within 0.8−1.3° of the ∠HOH^{max} values for water molecules, and the FWHM are very close. From the DFT-MD simulation results, brucite edge OH$_2$ groups have an angular ∠HOH distribution clearly distinct from that of water molecules, with a larger FWHM and an asymmetrical shape indicating at least two populations of OH$_2$ groups (Figure 4a), resulting in an average ∠HOH = 103.8°, which is 2.1° lower than the average ∠HOH value for water molecules. Interestingly, the ClayFF-orig and ClayFF-MOH ∠HOH distributions of OH$_2$ groups are distinct. While the ClayFF-orig distribution is very similar to that of molecular water, the ClayFF-MOH distribution has a lower ∠HOH^{max} resulting in an average angle of 102.6° and a broader width, both closer to the DFT distribution. These results validate the application of the flexible SPC model to OH$_2$ groups.

Orientation of Surface OH$_2$ Groups. Similar to our analysis of the surface OH orientation (Figures 4 and 5), the orientation of OH$_2$ groups on the edge surfaces of brucite and gibbsite is illustrated by the distribution of the O−H bond vectors projected on the crystallographic *xz* plane (Figure 8), with the O and H density profiles given additionally in Figure S9. Visualization of the distributions is facilitated by comparison with the DFT-MD snapshots in Figures 1c and 2c.

The DFT-MD-derived orientational distribution of the brucite edge surface O−H vectors reveals two main orientations comprising 84% of the total intensity: the spot "be$_I$" (54%) indicates an orientation predominately toward +z direction, while the spot "be$_{II}$" (30%) is due to the O−H orientations toward *x* (Figure 8a). The ratio of intensities between the spots "be$_I$" and "be$_{II}$" is 1.8:1 and remains nearly the same for the ClayFF-orig results (1.9:1) but with more
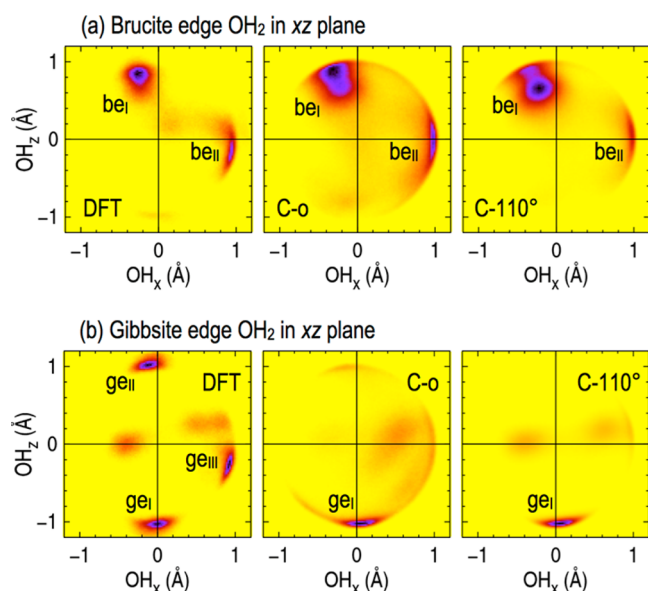
Figure 8. Orientation of gibbsite and brucite edge OH_2 groups: distribution of the O−H bond vectors projected on the xz plane. The color range from the lowest to the highest intensity is yellow, red, blue, and black. "C-o" and "C-110°" stand for ClayFF-orig and ClayFF-MOH-110°, respectively.

extended spot areas Figure 8a). With the ClayFF-MOH parametrization, secondary distributions decrease in intensity in favor of the two main orientations of which "be_I" is favored with a 4.5:1 ratio (Figure 8a).

For the gibbsite edge, the DFT-MD simulation produces three main orientations that account for 68% of the total intensity with comparable probabilities (Figure 8b). The spot "ge_I" (25%) is due to the O−H orientations toward −z, "ge_{II}" (22%) toward +x, and "ge_{III}" (21%) toward +z. The spot "ge_I" is also present in the C-MD distributions and represents 34% and 44% with ClayFF-orig and ClayFF-MOH models, respectively. However, the spot "ge_{II}" is almost absent from the C-MD distributions because it is largely due to the original OH groups becoming OH_2 groups after a proton hopping event, as illustrated in Figure 2c.

CONCLUSIONS

Zeitler et al.[49] have earlier introduced a Mg−O−H bending term for ClayFF, $E_{bend} = k (\theta - \theta_0)^2$, to better describe the structure and dynamics of hydroxyl groups at the surfaces of brucite, $Mg(OH)_2$. Here we used a more systematic approach based on vibrational frequencies and multiple structural criteria to determine the optimal values of the metal−O−H bending parameters θ_0 and k. This work was performed for the Al−O−H bending term considering the bulk crystal, the basal surface, and the (010) gibbsite edge surfaces. For consistency, the procedure was also applied to the Mg−O−H bending term which was first parametrized by Zeitler et al.,[49] based on the bulk crystal, the basal surface, and the (1$\bar{1}$0) brucite edge surface. The optimal values of θ_0 and k were then evaluated with MD simulations of the bulk model and several hydrated surfaces, by comparing the results of classical MD simulations with the original ClayFF-orig model and the improved ClayFF-MOH model to the results of DFT MD simulations.

We determined the optimal value of the Al−O−H force constant and equilibrium angle to be k_{AlOH} =

15 kcal mol^{-1} rad^{-2} and $\theta_{0,AlOH}$ = 110°. For the Mg−O−H bending term, we retained the value of k_{MgOH} = 6 kcal mol^{-1} rad^{-2} obtained by Zeitler et al.[49] Our analysis indicates that ClayFF-MOH with $\theta_{0,MgOH}$ = 110° provides the best results for the brucite edge surface and is applicable to the bulk and basal surface, therefore $\theta_{0,MgOH} = \theta_{0,AlOH}$ = 110° is selected. For brucite, the use of ClayFF-MOH instead of ClayFF-orig results in a more properly localized orientation of hydroxyl groups, in better agreement with DFT results, and strongly limits the desorption of OH_2 groups at the mineral edge. These properties are also improved by the ClayFF-MOH models for hydrated gibbsite interfaces where lattice parameters become closer to the experimental values and the topology of hydrogen bonding on the basal and edge surfaces are greatly improved.

Of course, all of these results assume that DFT calculations and the corresponding level of quantum theory provide the best standard to judge the suitability of a classical approach using ClayFF. The Mg−O−H and Al−O−H bending terms should be transferrable to most layered mineral models, but the optimal values obtained here for metal hydroxides will have to be evaluated for inclusion in mixed layer (e.g., T−O and T−O−T) models representative of clay minerals. Although an extensive comparison of structural properties was provided here, an analysis of the hydrogen bonding network and its statistical parameters as well as a detailed analysis of the vibrational behavior of the bulk and surface hydroxyl groups of brucite and gibbsite are beyond the scope of the current work and will be discussed elsewhere (Figure S10 illustrates the improvement brought by the addition of the M−O−H bending term for reproducing the librational spectra of the edge O−H groups. A similar parametrization of the M−O−H bending terms for Si and Al atoms in tetrahedral coordination, essentially completing the current stage of ClayFF improvements aimed at significantly more accurate and reliable modeling of clay particle surfaces and edges, will also be reported separately.

■ ASSOCIATED CONTENT

Ⓢ Supporting Information

The Supporting Information is available free of charge on the ACS Publications website at DOI: 10.1021/acs.jpcc.7b05362.

Additional comparisons between DFT and ClayFF-MOH, additional DFT-MD results, and implementation of ClayFF-MOH in LAMMPS (PDF)

■ AUTHOR INFORMATION

Corresponding Author
*E-mail: kalinich@subatech.in2p3.fr.

ORCID Ⓘ
Andrey G. Kalinichev: 0000-0003-0743-4242

Notes
The authors declare no competing financial interest.

■ ACKNOWLEDGMENTS

■ REFERENCES

(1) Cygan, R. T.; Liang, J.-J.; Kalinichev, A. G. Molecular Models of Hydroxide, Oxyhydroxide, and Clay Phases and the Development of a General Force Field. *J. Phys. Chem. B* **2004**, *108*, 1255−1266.

(2) Brown, G. E.; Henrich, V. E.; Casey, W. H.; Clark, D. L.; Eggleston, C.; Felmy, A.; Goodman, D. W.; Grätzel, M.; Maciel, G.; McCarthy, M. I.; et al. Metal Oxide Surfaces and Their Interactions with Aqueous Solutions and Microbial Organisms. *Chem. Rev.* **1999**, *99*, 77−174.

(3) Güven, N. Bentonites - Clays for Molecular Engineering. *Elements* **2009**, *5*, 89−92.

(4) *Handbook of Clay Science, Vol. 1*, Bergaya, F., Theng, B. K. G., Lagaly, G., Eds.; Developments in Clay Science; Elsevier B.V., 2006.

(5) Cygan, R. T.; Greathouse, J. A.; Heinz, H.; Kalinichev, A. G. Molecular Models and Simulations of Layered Materials. *J. Mater. Chem.* **2009**, *19*, 2470−2481.

(6) Teppen, B. J.; Rasmussen, K.; Bertsch, P. M.; Miller, D. M.; Schafer, L. Molecular Dynamics Modeling of Clay Minerals 0.1. Gibbsite, Kaolinite, Pyrophyllite, and Beidellite. *J. Phys. Chem. B* **1997**, *101*, 1579−1587.

(7) Bougeard, D.; Smirnov, K. S.; Geidel, E. Vibrational Spectra and Structure of Kaolinite: A Computer Simulation Study. *J. Phys. Chem. B* **2000**, *104*, 9210−9217.

(8) Sainz-Diaz, C. I.; Hernández-Laguna, A.; Dove, M. T. Modeling of Dioctahedral 2:1 Phyllosilicates by Means of Transferable Empirical Potentials. *Phys. Chem. Miner.* **2001**, *28*, 130−141.

(9) Sato, H.; Yamagishi, A.; Kawamura, K. Molecular Simulation for Flexibility of a Single Clay Layer. *J. Phys. Chem. B* **2001**, *105*, 7990−7997.

(10) Arab, M.; Bougeard, D.; Smirnov, K. S. Experimental and Computer Simulation Study of the Vibrational Spectra of Vermiculite. *Phys. Chem. Chem. Phys.* **2002**, *4*, 1957−1963.

(11) Heinz, H.; Castelijns, H. J.; Suter, U. W. Structure and Phase Transitions of Alkyl Chains on Mica. *J. Am. Chem. Soc.* **2003**, *125*, 9500−9510.

(12) Heinz, H.; Suter, U. W. Atomic Charges for Classical Simulations of Polar Systems. *J. Phys. Chem. B* **2004**, *108*, 18341−18352.

(13) Heinz, H.; Lin, T.-J.; Kishore Mishra, R.; Emami, F. S. Thermodynamically Consistent Force Fields for the Assembly of Inorganic, Organic, and Biological Nanostructures: The INTERFACE Force Field. *Langmuir* **2013**, *29*, 1754−1765.

(14) Kirkpatrick, R. J.; Kalinichev, A. G.; Bowers, G. M.; Yazaydin, A. O.; Krishnan, M.; Saharay, M.; Morrow, C. P. NMR and Computational Molecular Modeling Studies of Mineral Surfaces and Interlayer Galleries: A Review. *Am. Mineral.* **2015**, *100*, 1341−1354.

(15) Geysermans, P.; Noguera, C. Advances in Atomistic Simulations of Mineral Surfaces. *J. Mater. Chem.* **2009**, *19*, 7807−7821.

(16) Yan, L.; Englert, A. H.; Masliyah, J. H.; Xu, Z. Determination of Anisotropic Surface Characteristics of Different Phyllosilicates by Direct Force Measurements. *Langmuir* **2011**, *27*, 12996−13007.

(17) Bourg, I. C.; Sposito, G.; Bourg, A. C. M. Modeling the Acid−base Surface Chemistry of Montmorillonite. *J. Colloid Interface Sci.* **2007**, *312*, 297−310.

(18) Zhao, H.; Bhattacharjee, S.; Chow, R.; Wallace, D.; Masliyah, J. H.; Xu, Z. Probing Surface Charge Potentials of Clay Basal Planes and Edges by Direct Force Measurements. *Langmuir* **2008**, *24*, 12899−12910.

(19) Keren, R.; Sparks, D. L. The Role of Edge Surfaces in Flocculation of 2:1 Clay Minerals. *Soil Sci. Soc. Am. J.* **1995**, *59*, 430.

(20) Tombácz, E.; Szekeres, M. Colloidal Behavior of Aqueous Montmorillonite Suspensions: The Specific Role of pH in the Presence of Indifferent Electrolytes. *Appl. Clay Sci.* **2004**, *27*, 75−94.

(21) Bickmore, B. R.; Bosbach, D.; Hochella, M. F.; Charlet, L.; Rufe, E. In Situ Atomic Force Microscopy Study of Hectorite and Nontronite Dissolution: Implications for Phyllosilicate Edge Surface Structures and Dissolution Mechanisms. *Am. Mineral.* **2001**, *86*, 411−423.

(22) Decarreau, A.; Petit, S.; Andrieux, P.; Villieras, F.; Pelletier, M.; Razafitianamaharavo, A. Study of Low-Pressure Argon Adsorption on Synthetic Nontronite: Implications for Smectite Crystal Growth. *Clays Clay Miner.* **2014**, *62*, 102−111.

(23) Sondi, I.; Tomasic, V.; Filipovic-Vincekovic, N. Release of Silicon and Aluminum from Montmorillonite Surfaces in Aqueous Systems. *Croat. Chem. Acta* **2008**, *81*, 623−629.

(24) Marty, N. C. M.; Cama, J.; Sato, T.; Chino, D.; Villieras, F.; Razafitianamaharavo, A.; Brendle, J.; Giffaut, E.; Soler, J. M.; Gaucher, E. C.; et al. Dissolution Kinetics of Synthetic Na-Smectite. An Integrated Experimental Approach. *Geochim. Cosmochim. Acta* **2011**, *75*, 5849−5864.

(25) Rozalén, M. L.; Huertas, F. J.; Brady, P. V.; Cama, J.; García-Palma, S.; Linares, J. Experimental Study of the Effect of pH on the Kinetics of Montmorillonite Dissolution at 25 °C. *Geochim. Cosmochim. Acta* **2008**, *72*, 4224−4253.

(26) Dzene, L.; Tertre, E.; Hubert, F.; Ferrage, E. Nature of the Sites Involved in the Process of Cesium Desorption from Vermiculite. *J. Colloid Interface Sci.* **2015**, *455*, 254−260.

(27) Aung, L. L.; Tertre, E.; Petit, S. Effect of the Morphology of Synthetic Kaolinites on Their Sorption Properties. *J. Colloid Interface Sci.* **2015**, *443*, 177−186.

(28) Dähn, R.; Baeyens, B.; Bradbury, M. H. Investigation of the Different Binding Edge Sites for Zn on Montmorillonite Using P-EXAFS − The Strong/Weak Site Concept in the S2PNE SC/CE Sorption Model. *Geochim. Cosmochim. Acta* **2011**, *75*, 5154−5168.

(29) Soltermann, D.; Fernandes, M. M.; Baeyens, B.; Dähn, R.; Miehé-Brendlé, J.; Wehrli, B.; Bradbury, M. H. Fe(II) Sorption on a Synthetic Montmorillonite. A Combined Macroscopic and Spectroscopic Study. *Environ. Sci. Technol.* **2013**, *47*, 6978−6986.

(30) Marques Fernandes, M.; Baeyens, B.; Dähn, R.; Scheinost, A. C.; Bradbury, M. H. U(VI) Sorption on Montmorillonite in the Absence and Presence of Carbonate: A Macroscopic and Microscopic Study. *Geochim. Cosmochim. Acta* **2012**, *93*, 262−277.

(31) Dähn, R.; Scheidegger, A. M.; Manceau, A.; Schlegel, M. L.; Baeyens, B.; Bradbury, M. H.; Chateigner, D. Structural Evidence for the Sorption of Ni(II) Atoms on the Edges of Montmorillonite Clay Minerals: A Polarized X-Ray Absorption Fine Structure Study. *Geochim. Cosmochim. Acta* **2003**, *67*, 1−15.

(32) Schlegel, M. L.; Descostes, M. Uranium Uptake by Hectorite and Montmorillonite: A Solution Chemistry and Polarized EXAFS Study. *Environ. Sci. Technol.* **2009**, *43*, 8593−8598.

(33) Hattori, T.; Saito, T.; Ishida, K.; Scheinost, A. C.; Tsuneda, T.; Nagasaki, S.; Tanaka, S. The Structure of Monomeric and Dimeric Uranyl Adsorption Complexes on Gibbsite: A Combined DFT and EXAFS Study. *Geochim. Cosmochim. Acta* **2009**, *73*, 5975−5988.

(34) Vasconcelos, I. F.; Haack, E. A.; Maurice, P. A.; Bunker, B. A. EXAFS Analysis of cadmium(II) Adsorption to Kaolinite. *Chem. Geol.* **2008**, *249*, 237−249.

(35) Schlegel, M. Polarized EXAFS Characterization of the Sorption Mechanism of Yttrium on Hectorite. *Radiochim. Acta* **2008**, *96*, 667−672.

(36) Churakov, S. V.; Gimmi, T. Up-Scaling of Molecular Diffusion Coefficients in Clays: A Two-Step Approach. *J. Phys. Chem. C* **2011**, *115*, 6703−6714.

(37) Croteau, T.; Bertram, A. K.; Patey, G. N. Adsorption and Structure of Water on Kaolinite Surfaces: Possible Insight into Ice

Nucleation from Grand Canonical Monte Carlo Calculations. *J. Phys. Chem. A* **2008**, *112*, 10708−10712.

(38) Croteau, T.; Bertram, A. K.; Patey, G. N. Simulation of Water Adsorption on Kaolinite under Atmospheric Conditions. *J. Phys. Chem. A* **2009**, *113*, 7826−7833.

(39) Croteau, T.; Bertram, A. K.; Patey, G. N. Water Adsorption on Kaolinite Surfaces Containing Trenches. *J. Phys. Chem. A* **2010**, *114*, 2171−2178.

(40) Ockwig, N. W.; Greathouse, J. A.; Durkin, J. S.; Cygan, R. T.; Daemen, L. L.; Nenoff, T. M. Nanoconfined Water in Magnesium-Rich 2:1 Phyllosilicates. *J. Am. Chem. Soc.* **2009**, *131*, 8155−8162.

(41) Du, H.; Miller, J. D. A Molecular Dynamics Simulation Study of Water Structure and Adsorption States at Talc Surfaces. *Int. J. Miner. Process.* **2007**, *84*, 172−184.

(42) Nalaskowski, J.; Abdul, B.; Du, H.; Miller, J. d. Anisotropic Character of Talc Surfaces as Revealed by Streaming Potential Measurements, Atomic Force Microscopy, Molecular Dynamics Simulations and Contact Angle Measurements. *Can. Metall. Q.* **2007**, *46*, 227−235.

(43) Ebrahimi, D.; Whittle, A. J.; Pellenq, R. J.-M. Mesoscale Properties of Clay Aggregates from Potential of Mean Force Representation of Interactions between Nanoplatelets. *J. Chem. Phys.* **2014**, *140*, 154309.

(44) Martins, D. M. S.; Molinari, M.; Gonçalves, M. A.; Mirão, J. P.; Parker, S. C. Toward Modeling Clay Mineral Nanoparticles: The Edge Surfaces of Pyrophyllite and Their Interaction with Water. *J. Phys. Chem. C* **2014**, *118*, 27308−27317.

(45) Newton, A. G.; Sposito, G. Molecular Dynamics Simulations of Pyrophyllite Edge Surfaces: Structure, Surface Energies, and Solvent Accessibility. *Clays Clay Miner.* **2015**, *63*, 277−289.

(46) Newton, A. G.; Kwon, K. D.; Cheong, D.-K. Edge Structure of Montmorillonite from Atomistic Simulations. *Minerals* **2016**, *6*, 25.

(47) Churakov, S. V. Ab Initio Study of Sorption on Pyrophyllite: Structure and Acidity of the Edge Sites. *J. Phys. Chem. B* **2006**, *110*, 4135−4146.

(48) Yu, K.; Schmidt, J. R. Elucidating the Crystal Face- and Hydration-Dependent Catalytic Activity of Hydrotalcites in Biodiesel Production. *J. Phys. Chem. C* **2011**, *115*, 1887−1898.

(49) Zeitler, T. R.; Greathouse, J. A.; Gale, J. D.; Cygan, R. T. Vibrational Analysis of Brucite Surfaces and the Development of an Improved Force Field for Molecular Simulation of Interfaces. *J. Phys. Chem. C* **2014**, *118*, 7946−7953.

(50) Catti, M.; Ferraris, G.; Hull, S.; Pavese, A. Static Compression and H-Disorder in Brucite, Mg(OH)2, to 11 GPa - a Powder Neutron-Diffraction Study. *Phys. Chem. Miner.* **1995**, *22*, 200−206.

(51) Demichelis, R.; Noel, Y.; Ugliengo, P.; Zicovich-Wilson, C. M.; Dovesi, R. Physico-Chemical Features of Aluminum Hydroxides As Modeled with the Hybrid B3LYP Functional and Localized Basis Functions. *J. Phys. Chem. C* **2011**, *115*, 13107−13134.

(52) Nagendran, S.; Periyasamy, G.; Kamath, P. V. DFT Study of Polymorphism in Al(OH)3: A Structural Synthon Approach. *Z. Anorg. Allg. Chem.* **2015**, *641*, 2396−2403.

(53) Peintinger, M. F.; Kratz, M. J.; Bredow, T. Quantum-Chemical Study of Stable, Meta-Stable and High-Pressure Alumina Polymorphs and Aluminum Hydroxides. *J. Mater. Chem. A* **2014**, *2*, 13143−13158.

(54) Saalfeld, H.; Wedde, M. Refinement of Crystal-Structure of Gibbsite, Al(OH)3. *Z. Kristallogr.* **1974**, *139*, 129−135.

(55) Wang, S. L.; Johnston, C. T. Assignment of the Structural OH Stretching Bands of Gibbsite. *Am. Mineral.* **2000**, *85*, 739−744.

(56) Rzhevskii, A. M.; Ribeiro, F. H. UV Raman Spectroscopic Study of Hydrogen Bonding in Gibbsite and Bayerite between 93 and 453 K. *J. Raman Spectrosc.* **2001**, *32*, 923−928.

(57) Hiemstra, T.; Yong, H.; Van Riemsdijk, W. H. Interfacial Charging Phenomena of Aluminum (Hydr)oxides. *Langmuir* **1999**, *15*, 5942−5955.

(58) Liu, X.; Cheng, J.; Sprik, M.; Lu, X.; Wang, R. Understanding Surface Acidity of Gibbsite with First Principles Molecular Dynamics Simulations. *Geochim. Cosmochim. Acta* **2013**, *120*, 487−495.

(59) Pascale, F.; Tosoni, S.; Zicovich-Wilson, C.; Ugliengo, P.; Orlando, R.; Dovesi, R. Vibrational Spectrum of Brucite, Mg(OH)2: A Periodic Ab Initio Quantum Mechanical Calculation Including OH Anharmonicity. *Chem. Phys. Lett.* **2004**, *396*, 308−315.

(60) Hermansson, K.; Gajewski, G.; Mitev, P. D. Pressure-Induced OH Frequency Downshift in Brucite: Frequency-Distance and Frequency-Field Correlations. *J. Phys. Conf. Ser.* **2008**, *117*, 012018.

(61) Grimme, S. Semiempirical GGA-Type Density Functional Constructed with a Long-Range Dispersion Correction. *J. Comput. Chem.* **2006**, *27*, 1787−1799.

(62) Tunega, D.; Bucko, T.; Zaoui, A. Assessment of Ten DFT Methods in Predicting Structures of Sheet Silicates: Importance of Dispersion Corrections. *J. Chem. Phys.* **2012**, *137*, 114105.

(63) Perdew, J. P.; Burke, K.; Ernzerhof, M. Generalized Gradient Approximation Made Simple. *Phys. Rev. Lett.* **1996**, *77*, 3865−3868.

(64) Santra, B.; Michaelides, A.; Scheffler, M. On the Accuracy of Density-Functional Theory Exchange-Correlation Functionals for H Bonds in Small Water Clusters: Benchmarks Approaching the Complete Basis Set Limit. *J. Chem. Phys.* **2007**, *127*, 184104.

(65) Grimme, S.; Antony, J.; Ehrlich, S.; Krieg, H. A Consistent and Accurate Ab Initio Parametrization of Density Functional Dispersion Correction (DFT-D) for the 94 Elements H-Pu. *J. Chem. Phys.* **2010**, *132*, 154104.

(66) Lin, I.-C.; Seitsonen, A. P.; Tavernelli, I.; Rothlisberger, U. Structure and Dynamics of Liquid Water from Ab Initio Molecular Dynamics—Comparison of BLYP, PBE, and revPBE Density Functionals with and without van Der Waals Corrections. *J. Chem. Theory Comput.* **2012**, *8*, 3902−3910.

(67) Bankura, A.; Karmakar, A.; Carnevale, V.; Chandra, A.; Klein, M. L. Structure, Dynamics, and Spectral Diffusion of Water from First-Principles Molecular Dynamics. *J. Phys. Chem. C* **2014**, *118*, 29401−29411.

(68) VandeVondele, J.; Krack, M.; Mohamed, F.; Parrinello, M.; Chassaing, T.; Hutter, J. Quickstep: Fast and Accurate Density Functional Calculations Using a Mixed Gaussian and Plane Waves Approach. *Comput. Phys. Commun.* **2005**, *167*, 103−128.

(69) VandeVondele, J.; Hutter, J. Gaussian Basis Sets for Accurate Calculations on Molecular Systems in Gas and Condensed Phases. *J. Chem. Phys.* **2007**, *127*, 114105.

(70) Goedecker, S.; Teter, M.; Hutter, J. Separable Dual-Space Gaussian Pseudopotentials. *Phys. Rev. B: Condens. Matter Mater. Phys.* **1996**, *54*, 1703−1710.

(71) Greathouse, J. A.; Durkin, J. S.; Larentzos, J. P.; Cygan, R. T. Implementation of a Morse Potential to Model Hydroxyl Behavior in Phyllosilicates. *J. Chem. Phys.* **2009**, *130*, 134713.

(72) Berendsen, H. J. C.; Postma, J. P. M.; Gunsteren, W. F.; van Hermans, J. Interaction Models for Water in Relation to Protein Hydration. In *Intermolecular Forces*; The Jerusalem Symposia on Quantum Chemistry and Biochemistry; Pullman, B., Ed.; Springer: Netherlands, 1981; pp 331−342.

(73) Teleman, O.; Jönsson, B.; Engström, S. A Molecular Dynamics Simulation of a Water Model with Intramolecular Degrees of Freedom. *Mol. Phys.* **1987**, *60*, 193−203.

(74) Gale, J. D.; Rohl, A. L. The General Utility Lattice Program (GULP). *Mol. Simul.* **2003**, *29*, 291−341.

(75) Schmidt, J.; VandeVondele, J.; Kuo, I.-F. W.; Sebastiani, D.; Siepmann, J. I.; Hutter, J.; Mundy, C. J. Isobaric−Isothermal Molecular Dynamics Simulations Utilizing Density Functional Theory: An Assessment of the Structure and Density of Water at Near-Ambient Conditions. *J. Phys. Chem. B* **2009**, *113*, 11959−11964.

(76) Plimpton, S. Fast Parallel Algorithms for Short-Range Molecular Dynamics. *J. Comput. Phys.* **1995**, *117*, 1−19.

(77) Martyna, G. J.; Klein, M. L.; Tuckerman, M. Nosé−Hoover Chains: The Canonical Ensemble via Continuous Dynamics. *J. Chem. Phys.* **1992**, *97*, 2635−2643.

(78) Parrinello, M.; Rahman, A. Polymorphic Transitions in Single Crystals: A New Molecular Dynamics Method. *J. Appl. Phys.* **1981**, *52*, 7182−7190.

(79) Zigan, F.; Rothbauer, R. Neutronenbeugungsmessungen am Brucit. *Neues Jahrb. Für Mineral. - Monatshefte* **1967**, 137−143.

(80) Desgranges, L.; Calvarin, G.; Chevrier, G. Interlayer Interactions in M(OH)2: A Neutron Diffraction Study of Mg(OH)2. *Acta Crystallogr., Sect. B: Struct. Sci.* **1996**, *52*, 82−86.

(81) Parise, J.; Leinenweber, K.; Weidner, D.; Tan, K.; Vondreele, R. Pressure-Induced H-Bonding - Neutron-Diffraction Study of Brucite, Mg(OD)2, to 9.3 GPa. *Am. Mineral.* **1994**, *79*, 193−196.

(82) Mookherjee, M.; Stixrude, L. High-Pressure Proton Disorder in Brucite. *Am. Mineral.* **2006**, *91*, 127−134.

(83) Raugei, S.; Silvestrelli, P. L.; Parrinello, M. Pressure-Induced Frustration and Disorder in Mg(OH)2 and Ca(OH)2. *Phys. Rev. Lett.* **1999**, *83*, 2222−2225.

(84) Jodin-Caumon, M.-C.; Humbert, B.; Phambu, N.; Gaboriaud, F. A Vibrational Study of the Nature of Hydroxyl Groups Chemical Bonding in Two Aluminium Hydroxides. *Spectrochim. Acta, Part A* **2009**, *72*, 959−964.

(85) Ichikawa, K.; Kameda, Y.; Yamaguchi, T.; Wakita, H.; Misawa, M. Neutron-Diffraction Investigation of the Intramolecular Structure of a Water Molecule in the Liquid Phase at High Temperatures. *Mol. Phys.* **1991**, *73*, 79−86.

Structure of Hydrated Gibbsite and Brucite Edge Surfaces:

DFT Results and Further Development of the ClayFF Classical Force Field

with Metal-O-H Angle Bending Terms

Supporting information

Maxime Pouvreau,[†] Jeffery A. Greathouse,[‡] Randall T. Cygan[‡], and Andrey G. Kalinichev,[*,†]

[†]Laboratoire SUBATECH (UMR 6457), Institut Mines-Télécom Atlantique, 44307 Nantes, France

[‡]Geochemistry Department, Sandia National Laboratories, P.O Box 5800, MS 0754, Albuquerque, NM, 87185-0754, USA

[*] Corresponding Author: kalinich@subatech.in2p3.fr

I. RESULTS FROM STATIC CALCULATIONS

In Figs. S1-S6, the mean differences between the DFT and ClayFF-MOH results in terms of wavenumbers and O-H orientations are represented against the Metal-O-H bending term parameters θ_0 and k, for every value of θ_0 within the 90-130° range ($\delta\theta = 1°$), and for every value of k within the 0-40 kcal·mol^{-1}·rad^{-2} range ($\delta k = 1°$).

For each DFT-derived mode u, the ClayFF-MOH-derived mode v_0 corresponding to the maximum value of the overlap, S_{u,v_0}, was found (S1). The overlap S_{u,v_0} was then used to weight the difference in wavenumbers $\left| \bar{v}_u - \bar{v}_{v_0} \right|$ (S2).

$$S_{u,v_0} = \max_{\text{modes } v} \left\{ \sum_{i=1}^{N_{\text{atoms}}} \boldsymbol{e}_{u,i} \cdot \boldsymbol{e}_{v,i} \right\} \tag{S1}$$

$$\langle |\Delta\bar{v}| \rangle = \frac{1}{\sum_{i=1}^{N_{\text{modes}}} S_{u,v_0}} \sum_{i=1}^{N_{\text{modes}}} S_{u,v_0} \left| \bar{v}_u - \bar{v}_{v_0} \right| \tag{S2}$$

The average difference in O-H orientation was defined as:

$$\langle |\Delta O\text{-}H\ orientation| \rangle = \frac{1}{N_{\text{OH}}} \sum_{i=1}^{N_{\text{atoms}}} \arccos \left(\frac{\overrightarrow{OH}_{u,i} \cdot \overrightarrow{OH}_{v,i}}{\left\| \overrightarrow{OH}_{u,i} \right\| \cdot \left\| \overrightarrow{OH}_{v,i} \right\|} \right) \tag{S3}$$

All atoms are taken into account in the averaging for the bulk models. Only the outermost slice of atoms of each type are taken into account for the surface models: metal atoms, oxygen and hydrogen atoms of hydroxyl groups, as well as oxygen and hydrogen atoms of OH$_2$ groups for the edge surface models.

In order to define optimal areas in the (θ_0, k) plane, each point I of the graphs in Figs S1-S5, defined by its coordinates (θ_0, k, $\langle|\Delta\bar{v}|\rangle$) or ($\theta_0$, k, $\langle|\Delta O\text{-}H\ orientation|\rangle$), is assigned a small circle if:

$$\langle|\Delta A_I|\rangle - SEM(|\Delta A_I|) < \langle|\Delta A_{I_0}|\rangle - SEM(\Delta A_{I_0}) \tag{S4}$$

with *SEM* the standard error of the mean and I_0 the point of the graph corresponding to the minimum value of the mean difference in wavenumbers or in O-H orientation across the domain defined by $\theta_0 \epsilon$ [90;130°] and $k \epsilon$ [0;40 kcal·mol^{-1}·rad^{-2}].
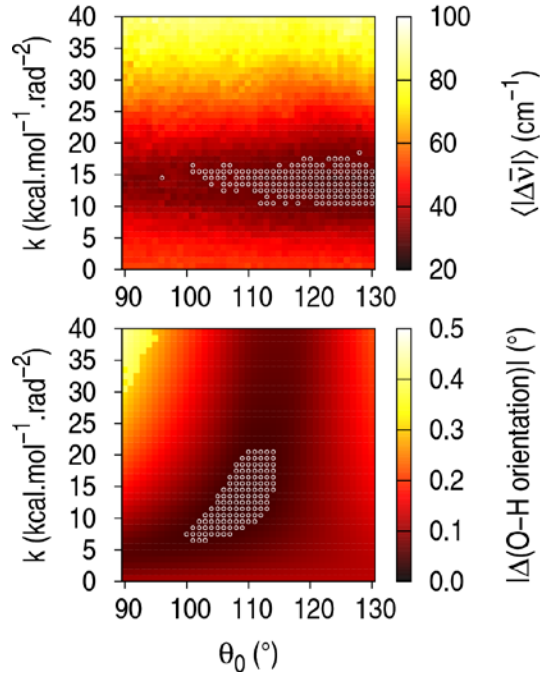
Figure S1. Gibbsite bulk

3
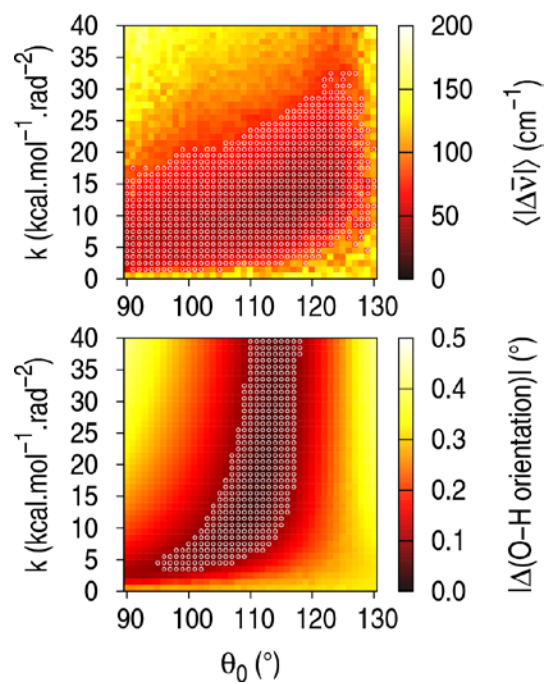
Figure S2. Gibbsite basal surface
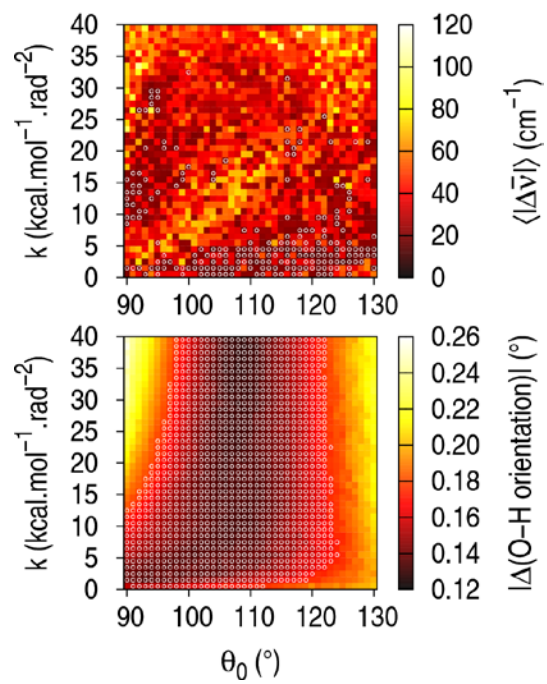
Figure S3. Gibbsite edge surface
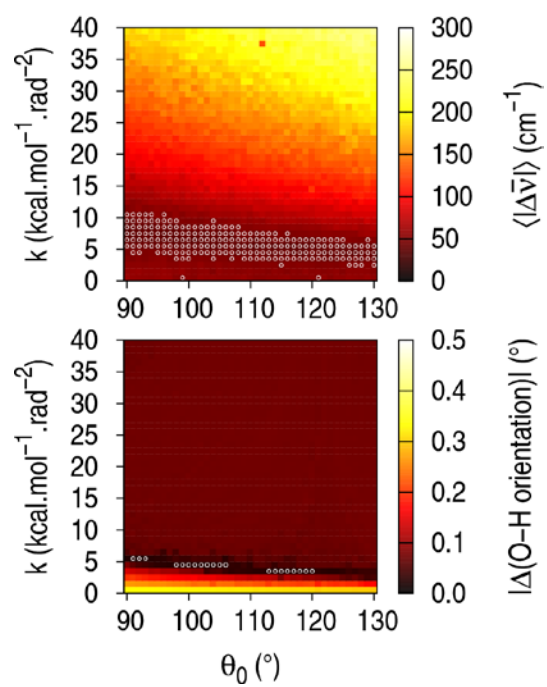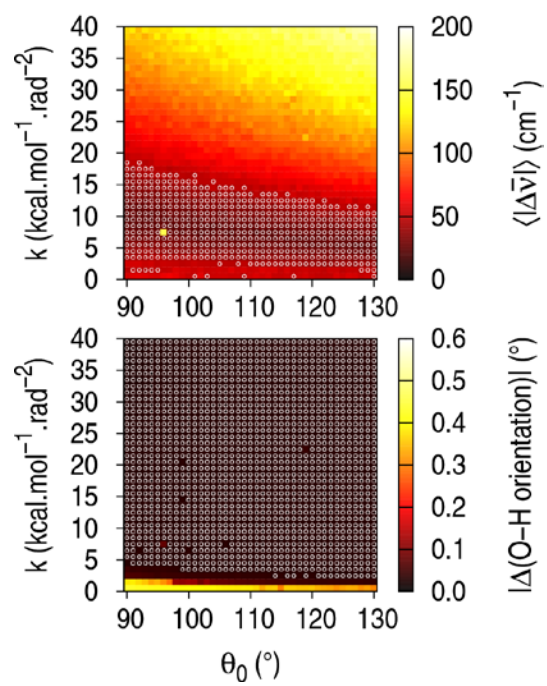
Figure S4. Brucite bulk
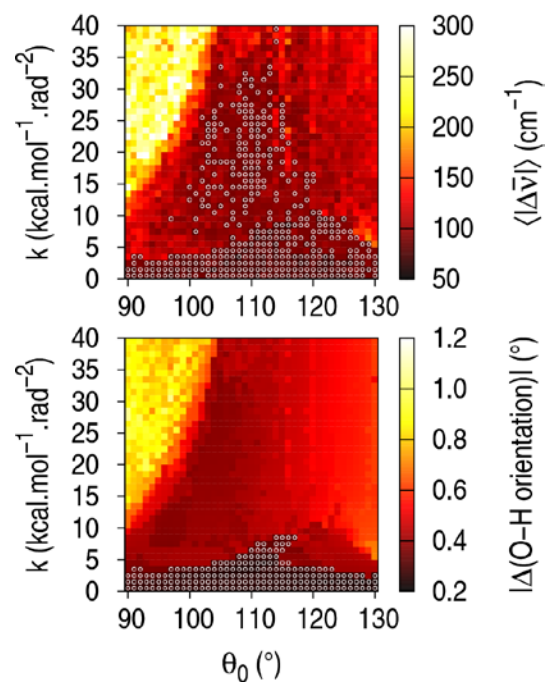

Figure S5. Brucite basal surface

Figure S6. Brucite edge surface

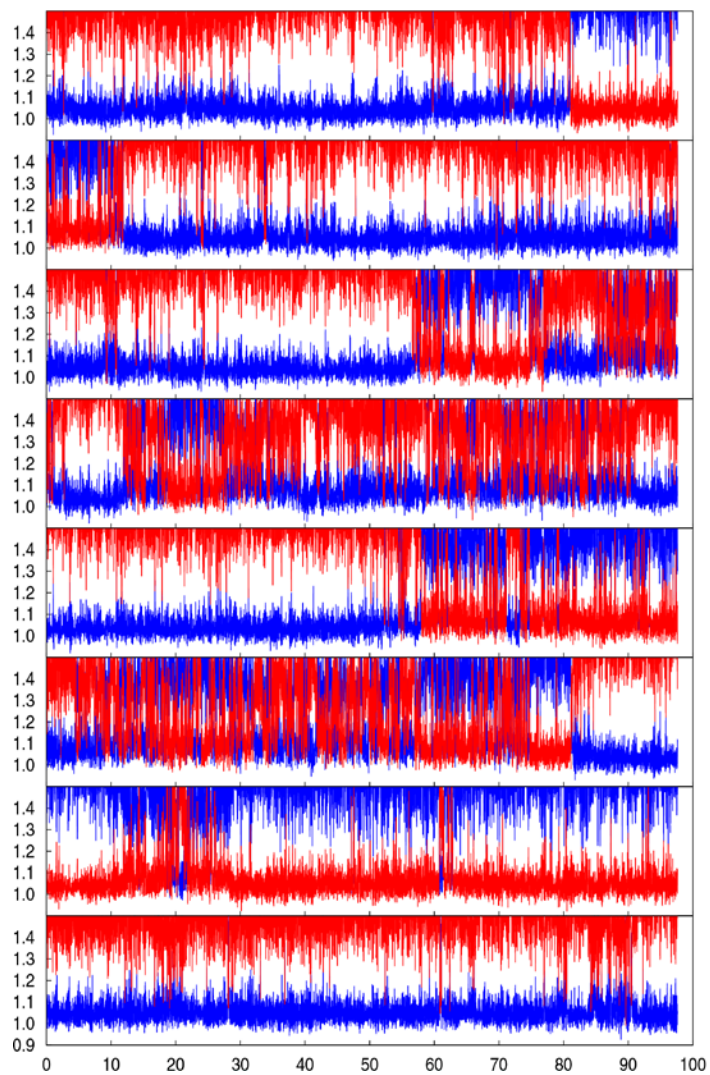## II. COMPLEMENTARY MD-DERIVED RESULTS

Figure S7. Evolution of the distance (Å) between a proton and its 2 closest O neighbors on the edge surface of gibbsite as a function of time (ps), for a selection of 8 protons, during the DFT-MD run.
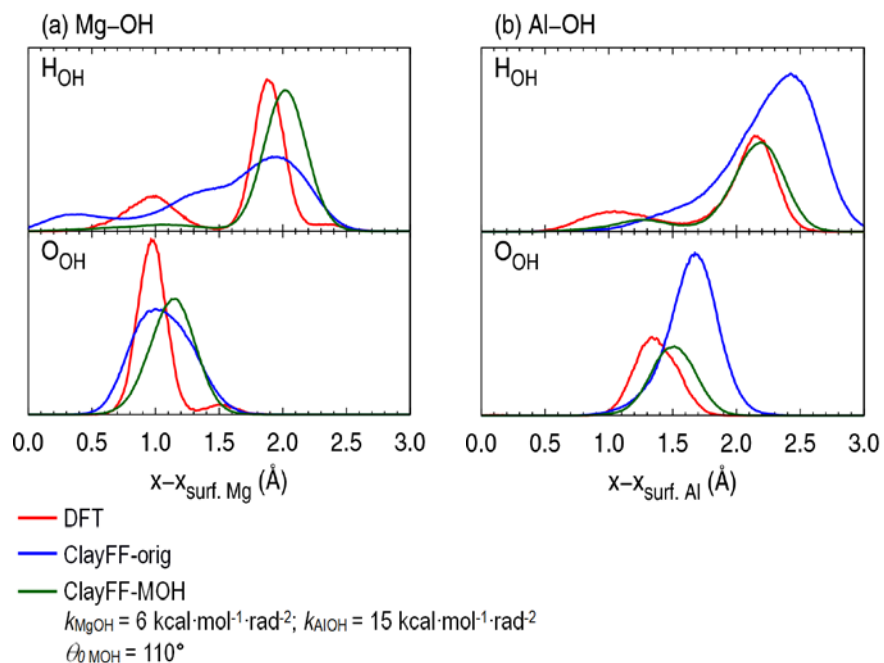
Figure S8. Density profiles of the atoms of the edge hydroxyl groups. (a) brucite edge surface and (b) gibbsite edge surface. x is normal to the edge plane.
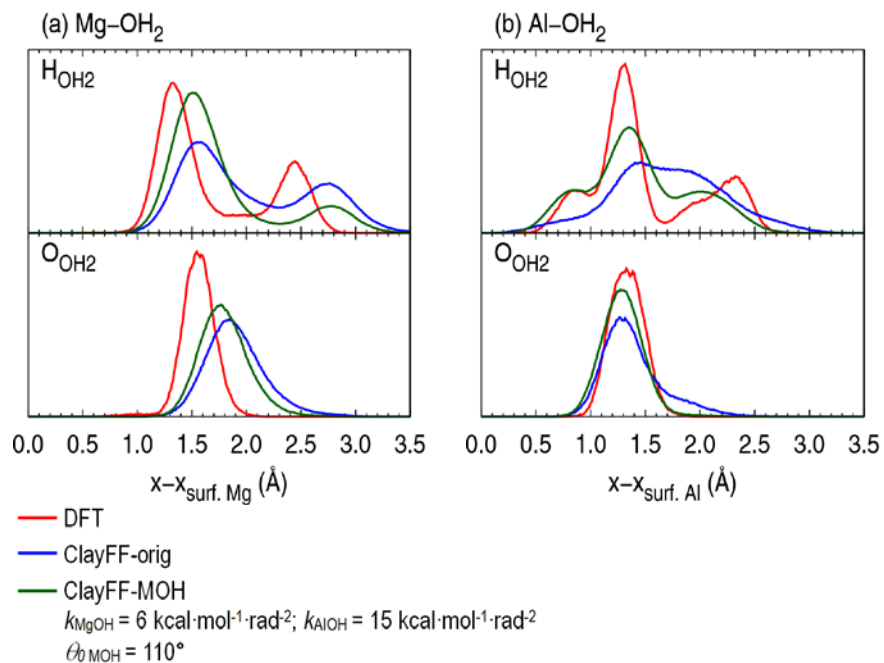

Figure S9. Density profiles of the atoms of the edge OH_2 groups. (a) brucite edge surface and (b) gibbsite edge surface. x is normal to the edge plane.

(a) Brucite H_{OH}

(b) Gibbsite H_{OH}

— DFT
— ClayFF-orig
— ClayFF-MOH
k_{MgOH} = 6 kcal·mol⁻¹·rad⁻²; k_{AlOH} = 15 kcal·mol⁻¹·rad⁻²
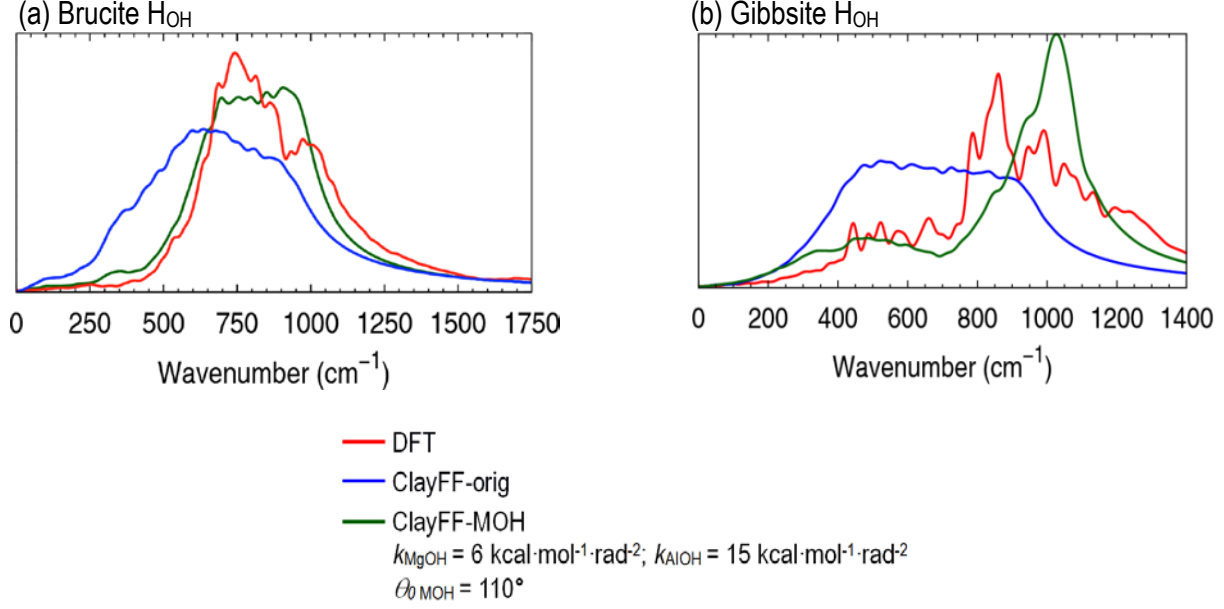$\theta_{0\ MOH}$ = 110°

Figure S10. Vibrational density of states of the hydrogen atoms of the OH groups belonging to the edge surfaces of brucite and gibbsite.

In Fig. S10 above the vibrational density of states is calculated from the velocity autocorrelation function $f(t)$ of the hydrogen atoms. The function $f'(t)$ is then obtained by windowing $f(t)$, with the upper bound set to t_{win}=1 ps:

$$f'(t) = f(t)\sqrt{1 - \frac{t}{t_{win}}} \tag{S4}$$

The vibrational density of states $P(v)$ is then calculated:

$$P(v) = \int [(f'(t)\cos(\omega t))^2 + (f'(t)\sin(\omega t))^2]\, dt \tag{S5}$$

III. Implementation of the new M-O-H ClayFF term in LAMMPS

9

The Metal-O-H angle potential must be added to the ClayFF force field by keeping active the Metal-O and Metal-H nonbonded—Lennard-Jones and coulombic—interactions.

In the LAMMPS software, an angle potential can act on an A-B-C trio independently of the existence of A-B and B-C bonds. The M-O-H trios have to be generated beforehand by the user and have to be listed in LAMMPS under the "Angles" section of the data file with the following syntax: "*ID type atom1 atom2 atom3*", with one line per trio. In the input file, the line "angle_style harmonic**"** must be included. Angle coefficients are defined either in the input file with "angle_coeff *type k θ_0*" or in the data file with "*type k θ_0*" under the "Angle Coeffs" section. Since no M-O bond is defined in ClayFF, LAMMPS will keep turned on the Lennard-Jones and coulombic interactions between M and O atoms, and between M and H atoms, which is the wanted behavior.

If MD software is used where M-O-H angles can only be generated automatically from the M-O and O-H connections, then the user has to ensure the software is able to turn on the nonbonded M-O and M-H terms—while keeping turned off the intramolecular H-H and O-H nonbonded terms for water molecules.